The Solar Neighborhood. XLVI. Revealing New M Dwarf Binaries and Their Orbital Architectures

Eliot Halley Vrijmoet[1,2,4] , Todd J. Henry[2,4] , Wei-Chun Jao[1,4] , and Serge B. Dieterich[2,3,4]
[1] Department of Physics and Astronomy, Georgia State University, Atlanta, GA 30303, USA; vrijmoet@astro.gsu.edu
[2] RECONS Institute, Chambersburg, PA 17201, USA
[3] Space Telescope Science Institute, 3700 San Martin Dr., Baltimore, MD 21218, USA
Received 2020 August 4; revised 2020 August 28; accepted 2020 August 31; published 2020 October 23

Abstract

We use 20 yr of astrometric data from the REsearch Consortium On Nearby Stars (RECONS) program on the Cerro Tololo Inter-American Observatory/SMARTS 0.9 m telescope to provide new insight into multiple star systems in the solar neighborhood. We provide new and updated parallaxes for 210 systems and derive nine high-quality astrometric orbits with periods of 2.49–16.63 yr. Using a total of 542 systems' parallaxes from RECONS, we compare systems within 25 pc to Gaia DR2 to define criteria for selecting unresolved astrometric multiples from the DR2 results. We find that three out of four unresolved multistar red dwarf systems within 25 pc in DR2 have `parallax_error` ⩾ 0.32 mas, `astrometric_gof_al` ⩾ 56, `astrometric_excess_noise_sig` ⩾ 108.0, `ruwe` ⩾ 2.0, and parallaxes more than ∼10% different from the long-term RECONS results. These criteria have broad applications to any work targeting nearby stars, from studies seeking binary systems to efforts targeting single stars for planet searches.

Unified Astronomy Thesaurus concepts: Astrometric binary stars (79); Astrometry (80); M stars (985); Trigonometric parallax (1713); Low mass stars (2050); Binary stars (154)

Supporting material: machine-readable tables

1. Introduction

The orbit of a binary star pair provides a host of useful information about the system, but many such orbits, when considered together, add another dimension to their utility by providing statistical clues to the formation and evolution of these systems. The size and shape of any orbit we observe today is the product of a suite of processes pertaining to dynamical gravitational interactions, magnetic fields, radiative feedback, and gas dynamics and accretion (for a thorough review, see Bate 2015). The balance of these processes depends on the initial conditions at formation, including the initial stellar masses, their angular momenta, and ultimately, the environment of the molecular cloud that led to these configurations.

Untangling the roles and dependencies of each of these processes requires assembling a representative set of observed multistar systems to which we can compare models of multiple star formation mechanisms (e.g., Bate 2012). Such observational results would also provide realistic inputs for multistar evolution modeling (e.g., Parker & Meyer 2014). These applications have been well covered for solar-type and more massive stars, most notably by Moe & Di Stefano (2017). At the low-mass end of the stellar main sequence, the red dwarf systems, also known as M dwarfs, represent a particularly important application because they span a factor of 8 in mass (0.08–0.62 $M_\odot$; Benedict et al. 2016) and, consequently, display a wide range of complex effects on their surfaces and interiors. This is evident in their remarkable scatter in luminosity at optical wavelengths (Clements et al. 2017). The distribution of separations of stars in red dwarf binaries has been observed to peak at a few tens of au (Winters et al. 2019), hinting at the distribution of their semimajor axes and thus orbital periods (Moe 2019), but statistics derived from true

orbits remain largely as described in the review of Duchêne & Kraus (2013). Hence, the goal of our work is to assemble a rich set of orbits that, when taken together, can constrain the formation and evolution models of stellar multiples for these complicated low-mass stars in particular. This paper represents the beginning of that effort.

The challenge of measuring M dwarf orbits has long been these systems' intrinsic faintness. This faintness has prevented the late M dwarfs in particular from being observable with most spectroscopic instruments until recently (e.g., Alonso-Floriano et al. 2015; Winters et al. 2020). The diminutive masses of these stars also increase the orbital period for a given semimajor axis, so observing orbits larger than a few au requires a decades-long time commitment for the smallest M dwarfs. For many instruments, these targets must also be restricted to within a few dozen parsecs to ensure all are sufficiently bright.

The REsearch Consortium On Nearby Stars[5] (RECONS) has been observing M dwarfs within 25 pc since 1999 via astrometry and photometry at Cerro Tololo Inter-American Observatory (CTIO). Astrometric observations of these systems provide a beautiful complement to spectroscopic observations, as these methods are sensitive to different types of binaries (different mass ratios and separations). Furthermore, astrometry can achieve comparable signal-to-noise ratios with less light, so high-quality observations can be obtained on systems as faint as *VRI* 22 mag using a small-aperture telescope such as the CTIO/SMARTS 0.9 m. With these benefits of the method and an observational program that has been observing the same set of stars for as long as 20 yr, in this work, RECONS is creating a catalog of multistar system orbits that will complement existing work in a way that is critically important for these small stars in particular.

---

[5] www.recons.org

In this paper, we present several orbits from our ongoing astrometry program at CTIO, representing the first infusion of M dwarf orbits for a broader project, described in Section 2. The sample of systems in our observing program is described in Section 3, and the astrometric observations and reductions are summarized in Section 4. Because every astrometric orbit is built upon accurate characterization of the system's parallactic and proper motions, Section 5 presents 210 systems' new or updated trigonometric parallaxes from our long-term program, and Section 6 presents nine astrometric orbits. In Section 7 we compare 542 of our ground-based parallax results to those of the space-based Gaia mission's Data Release 2 (DR2; Gaia Collaboration et al. 2018) and establish four criteria to select likely unresolved multistar systems from DR2, which could benefit any work that intends to target (or, alternatively, avoid) unresolved multiples among nearby red dwarfs. Future work, including observations of these systems to map orbits for this project, is briefly discussed in Section 8. Our conclusions are summarized in Section 9.

2. Orbital Architectures Project

The larger project launched by this work, dubbed the Orbital Architectures project, intends to bring together ∼120 M dwarf orbits to establish the distributions of orbital periods and eccentricities for massive, intermediate, and low-mass M dwarfs. Because these structures are the end results of billions of years of dynamical evolution compounded on their configurations at formation, this study of orbits provides several quantities that directly constrain key aspects of stellar formation models. The fraction of systems that form multiple stars (i.e., multiplicity) is the end product of the number of stars produced by each stellar core via fragmentation, modulated by the influences of magnetic fields, radiative feedback, and the dynamical environment during evolution (Duchêne & Kraus 2013). The deeper statistical properties of these systems, such as their distributions of mass ratios, separations, periods, and eccentricities, constrain dominant processes in their formation. Observations are often used to inform inputs to star cluster formation models, with the outputs compared to additional observations to evaluate the models' validity. Also notable is that the more unusual multistar configurations observed act as crucial tests for those formation models, as these outliers must not be ruled out as physically impossible.

Previous investigations into these distributions have primarily focused on solar-type stars (e.g., Duquennoy & Mayor 1991; Halbwachs et al. 2005). Attention turned to the M dwarfs mainly though efforts to determine their mass–luminosity relation (MLR; Henry & McCarthy 1993; Henry et al. 1999; Delfosse et al. 2000), and any investigations of their orbital distributions are usually presented as sidenotes. Udry et al. (2000) presented early results of a volume-limited all-sky search for M dwarf multiples with the CORAVEL spectrometers, forming a preliminary period-versus-eccentricity distribution using 13 of these systems supplemented by 17 from the literature. They noted evidence of a circularization timescale that matches that of G- and K-type stars, as well as hints of a paucity of circular orbits with long periods up to 20 yr. Although updates to this work have not been published, it remains a good starting point to which we can compare our study of stellar companions.

The M dwarfs' smaller masses, radii, and luminosities have also made them attractive targets for exoplanet searches across all major detection regimes: radial velocities with CARMENES (Quirrenbach et al. 2016), transits with the Transiting Exoplanet Survey Satellite (Ricker et al. 2014; Stassun et al. 2018), and direct imaging with the anticipated James Webb Space Telescope (Gardner et al. 2006) and the Nancy Grace Roman Space Telescope.[6] The M dwarfs' lower luminosities place their habitable zones closer to the stellar surface than those of larger stars, increasing the radial velocity semiamplitudes and probability of transits for those habitable planets. Their lower luminosities also benefit direct imaging observations by decreasing the star–planet contrast ratios. Reliable characterization of any detected exoplanets, however, depends critically upon precise information of their host stellar systems, including accurate stellar properties and identification of stars in the aperture (see, e.g., Fressin et al. 2013; Ciardi et al. 2015; Furlan et al. 2017). The significance of these effects (and the observing follow-up required) has inspired most surveys to carefully omit multistar systems from their samples of potential exoplanet hosts via extensive literature searches and sometimes even presurvey observations of potential targets (e.g., Cortés-Contreras et al. 2017). This step demonstrates the value of surveys that detect and characterize stellar multiples with a wide range of potential orbital diversity, in particular those surveys that combine different observational techniques to break free of any single method's limitations.

It is with these requirements in mind that we have begun this study of M dwarf systems' orbits. By assembling nearby systems from our own astrometry and later adding radial velocity studies and a new speckle interferometry program at the Southern Astrophysical Research (SOAR) Telescope (see Section 8), we will form a complete picture of M dwarf orbits out as far as 10 au while simultaneously representing all members of this expansive spectral type (from 0.08 to 0.62 $M_\odot$). This wide survey across stellar type as well as orbit size is the key element that will make this work useful for constraining formation and evolution models, as well as providing insight for upcoming exoplanet work.

3. Sample

The sample presented here is composed of red dwarfs within 25 pc visible from the southern sky. These limits are enforced as trigonometric parallax $\pi \geqslant 40$ mas, V-band absolute magnitude $9 \lesssim M_V \lesssim 24$, and declination $\delta \lesssim +30°$. Table 1 includes 210 systems (of 220 objects) for which we present new or updated parallaxes in this work. Those within 25 pc are also included in Table 2, along with many previously published parallaxes from RECONS, forming the sample of 582 targets that we compare with Gaia DR2. The absolute magnitude limits correspond to M dwarf mass limits of 0.08 and 0.62 $M_\odot$ using the MLR of Benedict et al. (2016) for the V band. For systems that have no reliable V-band photometry available, we instead require $5.3 \lesssim M_K \lesssim 12.0$ in the Two Micron All Sky Survey (2MASS) K_S band.

The growth of the sample has followed the growth of the RECONS observing program at the CTIO/SMARTS 0.9 m telescope, which began in 1999 under the auspices of the NOAO surveys program. With the goal of identifying "missing" members of the solar neighborhood, initial RECONS

---

[6] Formerly known as the Wide Field Infrared Survey Telescope, or WFIRST.

Table 1
New and Updated Results from the RECONS Astrometry Program

Name (1)	R.A. J2000.0 (2)	Decl. J2000.0 (3)	Filter (4)	N_{sea} (5)	N_{frm} (6)	Coverage (7)	Time (yr) (8)	N_{ref} (9)	π_{rel} (mas) (10)	π_{corr} (mas) (11)	π_{abs} (mas) (12)	μ (mas yr^{-1}) (13)	θ (deg) (14)	V_{tan} (km s^{-1}) (15)	Notes (16)
GJ 1001 A	00 04 36.46	−40 44 02.7	R	17 s	154	1999.64–2018.73	19.09	5	80.73 ± 1.64	1.03 ± 0.16	81.76 ± 1.65	1643.1 ± 0.30	156.6 ± 0.0	95.3	Update
LEHPM 1–0255	00 09 45.06	−42 01 39.6	V	5 c	66	2009.75–2018.70	8.95	5	55.89 ± 1.14	1.14 ± 0.22	57.03 ± 1.16	248.3 ± 0.40	90.5 ± 0.1	20.6	Update
GJ 2005 ABC	00 24 44.19	−27 08 24.2	R	21 s	189	1999.64–2019.74	20.10	6	116.73 ± 3.22	0.98 ± 0.04	117.71 ± 3.22	691.0 ± 0.50	350.7 ± 0.1	27.8	Update, PB
GJ 1012	00 28 39.46	−06 39 49.1	V	8 s	65	2012.96–2019.52	6.56	5	75.45 ± 2.36	1.11 ± 0.10	76.56 ± 2.36	862.6 ± 1.00	202.8 ± 0.1	53.4	
LP 050–078	00 31 04.25	−72 01 06.0	V	6 s	61	2014.93–2019.95	5.02	10	51.58 ± 1.14	0.91 ± 0.11	52.49 ± 1.15	436.0 ± 0.70	71.8 ± 0.2	39.4	
LP 645–053	00 35 44.13	−05 41 10.6	I	4 c	72	2015.55–2018.94	3.39	7	54.30 ± 0.92	0.96 ± 0.23	55.26 ± 0.95	265.0 ± 1.00	183.9 ± 0.3	22.7	
LHS 1134	00 43 26.01	−41 17 34.0	V	11 s	91	2009.78–2019.75	9.97	7	92.89 ± 1.20	1.95 ± 0.27	94.84 ± 1.23	764.4 ± 0.40	220.2 ± 0.1	38.2	Update, orbit
LHS 1140	00 44 59.34	−15 16 17.5	V	13 s	87	2003.95–2018.76	14.81	5	62.91 ± 1.64	0.61 ± 0.11	63.52 ± 1.64	669.6 ± 0.40	156.4 ± 0.1	50.0	Update
2MA 0045+1634	00 45 21.41	+16 34 44.7	I	7 s	27	2009.63–2019.76	10.13	8	63.34 ± 2.32	0.71 ± 0.16	64.05 ± 2.33	357.7 ± 0.50	96.9 ± 0.1	26.5	
2MA 0050–1538	00 50 24.42	−15 38 19.2	I	9 s	35	2010.73–2019.77	9.03	9	42.08 ± 1.66	0.43 ± 0.08	42.51 ± 1.66	519.2 ± 0.40	202.8 ± 0.1	57.9	
GJ 1025	01 00 56.37	−04 26 56.5	V	12 s	88	2000.57–2018.67	18.09	6	84.13 ± 1.44	0.57 ± 0.05	84.70 ± 1.44	1322.3 ± 0.20	70.4 ± 0.0	74.0	Update, PB
LTT 00573	01 01 24.65	−01 05 58.6	I	6 s	70	2013.94–2018.94	5.00	6	32.30 ± 1.18	2.88 ± 0.13	35.18 ± 1.19	278.5 ± 0.90	86.4 ± 0.3	37.5	
GJ 1028	01 04 53.81	−18 07 28.7	R	8 s	65	2012.95–2019.94	6.99	7	101.66 ± 1.27	1.21 ± 0.14	102.87 ± 1.28	1376.7 ± 0.60	69.8 ± 0.1	63.4	
SSS 0109–5100	01 09 01.51	−51 00 49.5	I	11 s	70	2009.75–2019.63	9.89	9	62.27 ± 0.72	1.04 ± 0.04	63.31 ± 0.72	222.8 ± 0.20	68.0 ± 0.1	16.7	
GJ 0054.1	01 12 30.65	−16 59 56.1	V	7 s	59	2003.85–2018.94	15.10	5	268.92 ± 4.30	1.67 ± 0.44	270.59 ± 4.32	1349.6 ± 1.00	62.7 ± 0.1	23.6	
DEN 0113–5429	01 13 16.41	−54 29 13.8	R	15 s	123	1999.91–2019.77	19.86	7	56.35 ± 0.79	1.62 ± 0.17	57.97 ± 0.81	390.0 ± 0.10	72.2 ± 0.0	31.9	Update, PB
G034–023	01 22 10.30	+22 09 02.7	V	4 c	54	2015.56–2018.93	3.37	7	84.29 ± 1.70	1.39 ± 0.16	85.68 ± 1.71	274.7 ± 1.50	123.1 ± 0.6	15.2	
LP 768–113	01 33 58.01	−17 38 23.8	R	9 s	73	2008.70–2019.76	11.06	5	68.22 ± 1.40	1.50 ± 0.50	69.72 ± 1.49	156.3 ± 0.60	167.8 ± 0.4	10.3	
2MA 0138–7320	01 38 21.52	−73 20 58.3	I	8 s	63	2009.74–2018.94	9.21	5	32.75 ± 1.32	0.14 ± 0.02	32.89 ± 1.32	123.9 ± 0.50	347.9 ± 0.4	17.9	
2MA 0141+1804	01 41 03.25	+18 04 50.1	I	6 s	26	2009.56–2015.93	6.37	6	40.16 ± 1.79	0.83 ± 0.10	40.99 ± 1.79	407.8 ± 1.00	97.4 ± 0.2	47.2	
L870–044 AB	01 46 36.84	−08 38 58.1	V	6 s	64	2013.67–2018.97	5.30	8	38.97 ± 1.75	0.81 ± 0.15	39.78 ± 1.76	448.0 ± 1.00	112.2 ± 0.2	53.4	PB
L088–043	01 53 37.08	−66 53 34.1	R	8 s	86	2005.71–2018.93	13.22	6	78.85 ± 3.20	2.97 ± 0.24	81.82 ± 3.21	420.0 ± 0.80	65.8 ± 0.2	24.3	Update
GJ 0083.1	02 00 12.96	+13 03 07.1	V	10 s	89	2010.74–2019.63	8.88	5	223.18 ± 2.00	1.57 ± 0.32	224.75 ± 2.03	2068.1 ± 0.60	148.3 ± 0.0	43.6	
LHS 1326	02 02 16.24	+10 20 13.9	V	13 s	59	2006.78–2019.93	13.15	5	108.10 ± 1.88	0.28 ± 0.03	108.38 ± 1.88	736.9 ± 0.50	248.3 ± 0.1	32.2	
LHS 1339	02 05 48.55	−30 10 36.0	V	15 s	98	2003.94–2019.75	15.81	5	105.55 ± 1.38	0.59 ± 0.07	106.14 ± 1.38	553.1 ± 0.30	280.9 ± 0.1	24.7	
LHS 1367	02 15 08.05	−30 40 01.3	I	8 s	58	2012.88–2019.93	7.05	5	71.16 ± 1.53	0.32 ± 0.03	71.48 ± 1.53	838.2 ± 0.60	115.0 ± 0.1	55.6	
LHS 1375	02 16 29.86	+13 35 12.7	V	11 s	78	2009.75–2019.94	10.20	8	105.65 ± 2.34	1.04 ± 0.26	106.69 ± 2.35	652.2 ± 1.00	130.9 ± 0.2	29.0	
2MA 0228+1639	02 28 42.44	+16 39 32.9	I	6 s	21	2010.75–2015.93	5.18	8	46.82 ± 3.14	0.65 ± 0.09	47.47 ± 3.14	582.9 ± 1.30	137.6 ± 0.2	58.2	
GJ 0102	02 33 37.18	+24 55 37.8	R	10 s	87	2010.74–2019.94	9.20	8	100.42 ± 2.76	1.49 ± 0.18	101.91 ± 2.77	671.6 ± 0.70	176.0 ± 0.1	31.2	
GJ 0105 B	02 36 04.91	+06 53 12.6	V	5 s	36	2010.97–2014.92	3.95	5	128.96 ± 4.93	1.05 ± 0.33	130.01 ± 4.94	2317.6 ± 3.40	51.2 ± 0.2	84.5	
LHS 0158	02 42 02.88	−44 30 58.7	I	5 c	86	2000.87–2010.00	9.13	10	19.11 ± 0.96	1.71 ± 0.12	20.82 ± 0.97	1007.8 ± 0.40	87.3 ± 0.0	229.4	Update
LP 993–115 BC	02 45 10.71	−43 44 32.4	V	14 s	105	1999.62–2018.96	19.33	9	77.79 ± 1.66	1.52 ± 0.10	79.31 ± 1.66	369.9 ± 0.20	174.8 ± 0.1	22.1	Update, PB
LP 771–021	02 48 41.01	−16 51 22.1	I	7 s	59	2012.95–2018.94	5.99	5	44.23 ± 1.28	0.70 ± 0.07	44.93 ± 1.28	281.7 ± 0.50	190.4 ± 0.2	29.7	
LHS 1491	03 04 04.49	−20 22 43.0	V	11 s	100	1999.71–2017.94	18.24	7	60.91 ± 0.97	0.96 ± 0.16	61.87 ± 0.98	684.8 ± 0.10	134.8 ± 0.0	52.5	Update
GJ 1057	03 13 22.92	+04 46 29.3	R	10 s	75	2009.93–2018.78	8.85	5	117.16 ± 1.66	1.33 ± 0.19	118.49 ± 1.67	1737.5 ± 0.50	87.4 ± 0.0	69.5	
2MA 0314+1603	03 14 03.44	+16 03 05.6	I	6 s	36	2010.97–2015.96	4.99	10	69.93 ± 1.45	1.07 ± 0.16	71.00 ± 1.46	251.7 ± 0.80	258.8 ± 0.3	16.8	
2MA 0314–0450	03 14 40.11	−04 50 31.8	I	6 s	27	2010.75–2015.97	5.22	6	27.44 ± 1.59	0.81 ± 0.10	28.25 ± 1.59	127.8 ± 0.70	224.3 ± 0.7	21.5	
SIP 0320–0446 AB	03 20 28.38	−04 46 36.7	I	11 s	49	2009.03–2018.78	9.76	9	46.42 ± 1.41	0.73 ± 0.04	47.15 ± 1.41	566.0 ± 0.40	205.0 ± 0.1	56.9	PB
L127–124	03 20 51.79	−63 51 52.5	V	6 s	60	2015.07–2019.95	4.88	8	53.68 ± 1.68	0.56 ± 0.04	54.24 ± 1.68	294.2 ± 0.90	183.8 ± 0.3	25.7	
L228–092	03 38 55.91	−52 34 10.7	R	6 s	79	2015.08–2019.93	4.85	7	81.64 ± 1.06	0.74 ± 0.06	82.38 ± 1.06	266.2 ± 0.70	32.7 ± 0.3	15.3	
LHS 1604	03 51 00.04	−00 52 44.9	I	9 s	59	2011.01–2019.75	8.74	8	66.67 ± 0.99	1.34 ± 0.09	68.01 ± 0.99	462.7 ± 0.40	178.7 ± 0.1	32.2	
2MA 0352+0210	03 52 10.86	+02 10 48.0	I	7 s	37	2009.73–2015.84	6.11	8	51.40 ± 1.74	0.77 ± 0.17	52.17 ± 1.75	458.7 ± 0.80	41.0 ± 0.2	41.7	
DEN 0354–1437	03 54 20.08	−14 37 38.8	I	7 s	67	2013.93–2019.93	6.00	5	48.94 ± 1.21	0.52 ± 0.13	49.46 ± 1.22	110.4 ± 0.80	320.7 ± 0.8	10.6	
UPM 0402–0242 A	04 02 32.39	−02 42 33.6	V	5 s	63	2014.80–2019.09	4.29	5	43.43 ± 2.17	0.83 ± 0.17	44.26 ± 2.18	54.3 ± 1.30	127.8 ± 2.6	5.8	
UPM 0402–0242 B	04 02 33.29	−02 42 16.2	V	5 s	65	2014.80–2019.09	4.29	5	44.34 ± 2.18	0.83 ± 0.17	45.17 ± 2.19	55.7 ± 1.30	137.4 ± 2.6	5.8	
LHS 1630 AB	04 07 20.50	−24 29 13.7	V	7 s	102	1999.71–2019.92	20.20	5	52.05 ± 1.08	1.74 ± 0.20	53.79 ± 1.10	681.2 ± 0.30	164.0 ± 0.0	60.0	Update

Table 1
(Continued)

Name (1)	R.A. J2000.0 (2)	Decl. J2000.0 (3)	Filter (4)	N_{sea} (5)	N_{frm} (6)	Coverage (7)	Time (yr) (8)	N_{ref} (9)	π_{rel} (mas) (10)	π_{corr} (mas) (11)	π_{abs} (mas) (12)	μ (mas yr^{-1}) (13)	θ (deg) (14)	V_{tan} (km s^{-1}) (15)	Notes (16)
GJ 0166 C	04 15 21.56	−07 39 21.2	V	10 s	76	2008.86–2019.92	11.07	6	204.31 ± 3.34	1.57 ± 0.34	205.88 ± 3.36	4088.6 ± 1.10	214.1 ± 0.0	94.1	
LHS 1668	04 24 56.19	−40 02 47.6	R	7 s	69	2013.80–2019.95	6.15	4	69.39 ± 1.05	1.67 ± 0.15	71.06 ± 1.06	648.0 ± 0.50	189.8 ± 0.1	43.2	
2MA 0429−3123 AB	04 29 18.43	−31 23 56.7	R	10 s	83	2003.95–2019.94	15.98	13	58.60 ± 1.05	0.72 ± 0.08	59.32 ± 1.05	122.5 ± 0.20	37.1 ± 0.2	9.8	Update, orbit
LP 775−031	04 35 16.14	−16 06 57.1	I	12 s	118	2003.95–2017.70	13.76	7	95.22 ± 0.78	0.82 ± 0.13	96.04 ± 0.79	356.7 ± 0.10	27.2 ± 0.0	17.6	Update, orbit
LP 655−043 ABC	04 38 02.52	−05 56 13.4	R	6 s	57	2003.95–2017.92	13.97	11	26.87 ± 1.25	1.33 ± 0.16	28.20 ± 1.26	188.7 ± 0.50	203.1 ± 0.3	31.7	
2MA 0445−3048	04 45 53.88	−30 48 20.8	I	11 s	54	2010.01–2019.95	9.94	9	61.98 ± 1.08	1.12 ± 0.11	63.10 ± 1.09	449.6 ± 0.30	160.3 ± 0.1	33.8	
LP 776−025	04 52 24.42	−16 49 22.2	V	6 s	65	2004.73–2019.92	15.19	8	66.31 ± 1.63	1.07 ± 0.09	67.38 ± 1.63	241.5 ± 0.30	151.3 ± 0.1	17.0	Update
LHS 1731	05 03 20.08	−17 22 25.0	V	16 s	246	1999.97–2017.06	17.08	9	106.60 ± 0.73	1.17 ± 0.11	107.77 ± 0.74	499.9 ± 0.10	207.6 ± 0.0	22.0	Update
GJ 0190 AB	05 08 35.05	−18 10 19.4	V	13 s	138	2004.83–2019.95	15.12	6	109.52 ± 2.11	1.63 ± 0.11	111.15 ± 2.11	1477.3 ± 0.50	161.0 ± 0.0	63.0	Orbit
L521−011	05 14 53.56	−33 04 30.0	I	8 s	64	2007.82–2018.78	10.96	10	21.77 ± 1.20	1.60 ± 0.11	23.37 ± 1.21	235.6 ± 0.50	56.0 ± 0.3	47.8	
LHS 0205	05 16 59.67	−78 17 20.2	V	8 s	69	2003.95–2019.10	15.15	7	67.81 ± 2.17	0.87 ± 0.25	68.68 ± 2.18	1133.4 ± 0.60	178.2 ± 0.0	78.2	Update
L449−001 AB	05 17 22.91	−35 21 54.7	V	13 c	170	2007.81–2019.75	11.93	7	85.42 ± 1.19	1.62 ± 0.24	87.04 ± 1.21	276.1 ± 0.30	233.8 ± 0.1	15.0	Update, PB
LP 892−032	05 18 36.63	−28 42 06.6	I	5 s	57	2016.05–2020.16	4.11	8	54.40 ± 1.13	0.69 ± 0.04	55.09 ± 1.13	443.1 ± 0.90	355.3 ± 0.2	38.1	
UPM 0531−0303 A	05 31 57.87	−03 03 36.8	V	4 c	63	2014.80–2018.08	3.28	9	24.42 ± 1.41	2.13 ± 0.22	26.55 ± 1.43	52.5 ± 1.20	164.0 ± 2.3	9.4	
UPM 0531−0303 B	05 31 57.87	−03 03 36.8	V	4 c	63	2014.80–2018.08	3.28	9	25.01 ± 0.68	2.13 ± 0.22	27.14 ± 0.71	51.7 ± 0.60	174.6 ± 1.0	9.0	
UPM 0531−0303 C	05 31 57.87	−03 03 36.8	V	4 c	63	2014.80–2018.08	3.28	9	26.84 ± 0.90	2.13 ± 0.22	28.97 ± 0.93	45.0 ± 0.80	173.3 ± 1.5	7.4	
GJ 0213	05 42 09.28	+12 29 21.8	V	9 s	88	2010.16–2018.78	8.61	6	172.27 ± 1.98	1.32 ± 0.38	173.59 ± 2.02	2534.7 ± 0.60	128.4 ± 0.0	69.2	
LP 837−037	05 53 55.39	−22 46 57.8	I	6 s	59	2015.07–2019.94	4.87	7	37.48 ± 0.88	0.38 ± 0.03	37.86 ± 0.88	264.0 ± 0.50	149.2 ± 0.2	33.0	
LHS 1810	06 02 54.24	−09 15 03.8	R	6 c	62	2014.92–2019.93	5.01	10	63.53 ± 1.09	1.11 ± 0.20	64.64 ± 1.11	608.5 ± 0.60	169.8 ± 0.1	44.6	
LHS 1823	06 08 16.44	−32 16 46.3	V	6 s	78	2014.93–2019.94	5.00	9	62.33 ± 1.00	0.77 ± 0.04	63.10 ± 1.00	730.5 ± 0.60	92.5 ± 0.1	54.9	
SCR 0613−2742 AB	06 13 13.31	−27 42 05.5	V	12 c	198	2007.82–2019.10	11.28	6	31.47 ± 0.70	1.68 ± 0.17	33.15 ± 0.72	13.7 ± 0.20	228.9 ± 1.7	2.0	Update, orbit
L308−057	06 21 06.66	−49 05 38.0	V	6 s	80	2015.06–2019.94	4.87	8	85.35 ± 0.92	0.68 ± 0.05	86.03 ± 0.92	251.5 ± 0.60	354.3 ± 0.2	13.9	
GJ 0232	06 24 41.29	+23 25 59.0	R	6 s	85	2010.16–2014.92	4.76	8	114.47 ± 1.87	1.74 ± 0.32	116.21 ± 1.90	746.2 ± 1.50	133.5 ± 0.2	30.4	
UPM 0632−0943	06 32 19.19	−09 43 29.1	R	5 c	66	2014.93–2019.09	4.15	9	39.25 ± 1.14	1.64 ± 0.28	40.89 ± 1.17	51.8 ± 0.70	194.5 ± 1.4	6.0	
L032−009 B	06 33 46.81	−75 37 29.9	V	16 c	227	2003.95–2018.97	15.02	6	115.66 ± 1.23	2.06 ± 0.23	117.72 ± 1.25	410.2 ± 0.30	308.1 ± 0.1	16.5	
L032−009 A	06 33 46.81	−75 37 29.9	V	16 c	231	2003.95–2018.97	15.02	6	115.52 ± 1.28	2.06 ± 0.23	117.58 ± 1.30	398.8 ± 0.30	312.6 ± 0.1	16.1	
NLTT 16977	06 43 29.79	−70 03 20.8	V	8 s	80	2009.93–2018.15	8.22	13	49.75 ± 1.06	0.64 ± 0.05	50.39 ± 1.06	186.7 ± 0.50	3.0 ± 0.2	17.6	
GJ 0250 B	06 52 18.05	−05 11 24.2	V	17 s	230	2003.96–2019.95	16.00	8	111.03 ± 1.37	1.36 ± 0.20	112.39 ± 1.38	574.5 ± 0.20	269.3 ± 0.0	24.2	
LP 661−013	06 56 18.95	−08 35 46.4	R	5 c	77	2013.94–2018.15	4.21	9	37.44 ± 1.00	1.39 ± 0.16	38.83 ± 1.01	236.1 ± 0.70	163.3 ± 0.3	28.8	
GJ 1093	06 59 28.81	+19 20 55.9	R	6 c	79	2009.94–2015.06	5.12	11	132.03 ± 1.28	0.62 ± 0.13	132.65 ± 1.29	1274.4 ± 0.70	134.3 ± 0.1	45.5	
SCR 0702−6102	07 02 50.34	−61 02 47.6	I	15 c	220	2003.84–2017.92	14.08	9	58.83 ± 0.56	1.29 ± 0.15	60.12 ± 0.58	786.6 ± 0.10	42.1 ± 0.0	62.0	Update, orbit
ESO 207−061	07 07 53.28	−49 00 50.4	I	7 c	67	2012.95–2018.94	5.99	13	41.23 ± 0.87	0.65 ± 0.06	41.88 ± 0.87	387.3 ± 0.40	358.3 ± 0.1	43.8	
SCR 0723−8015 AB	07 23 59.65	−80 15 17.8	I	13 s	166	2003.07–2020.14	17.06	8	59.06 ± 1.07	1.10 ± 0.15	60.16 ± 1.08	821.6 ± 0.20	330.4 ± 0.0	64.7	Update, PB
GJ 0273	07 27 24.50	+05 13 32.7	V	6 c	67	2010.01–2015.06	5.05	6	262.76 ± 3.83	0.83 ± 0.15	263.59 ± 3.83	3732.1 ± 2.20	171.2 ± 0.1	67.1	
LHS 1918 AB	07 28 13.09	−18 47 35.4	V	6 c	90	2014.81–2019.94	5.12	8	70.44 ± 0.88	1.35 ± 0.18	71.79 ± 0.90	606.0 ± 0.50	2.9 ± 0.1	40.0	PB
TYC 0777-141-1 AB	07 34 56.32	+14 45 54.2	V	4 c	69	2014.92–2017.95	3.03	8	57.98 ± 1.89	2.17 ± 0.28	60.15 ± 1.91	111.8 ± 1.80	216.4 ± 1.8	8.8	
GJ 0285	07 44 40.18	+03 33 08.9	V	6 s	77	2010.17–2015.06	4.89	9	170.07 ± 2.28	0.99 ± 0.16	171.06 ± 2.29	561.2 ± 1.50	218.8 ± 0.3	15.6	
LHS 1955 AB	07 54 54.80	−29 20 56.3	R	6 c	102	2000.94–2013.26	12.32	9	75.65 ± 0.88	1.60 ± 0.29	77.25 ± 0.93	598.1 ± 0.20	146.7 ± 0.0	36.7	Update
SCR 0757−7114	07 57 32.55	−71 14 53.8	V	7 s	69	2008.12–2019.95	11.83	9	41.91 ± 1.70	1.07 ± 0.12	42.98 ± 1.70	100.8 ± 0.50	86.8 ± 0.4	11.1	Update
LHS 2005 AB	08 22 47.45	−57 26 53.0	V	5 c	73	2016.05–2019.93	3.88	11	77.91 ± 1.11	2.05 ± 0.19	79.96 ± 1.13	597.4 ± 0.80	322.7 ± 0.1	35.4	
LHS 2005 C	08 22 47.87	−57 26 45.1	V	5 c	74	2016.05–2019.93	3.88	12	78.90 ± 1.11	2.05 ± 0.19	80.95 ± 1.13	564.4 ± 0.80	320.3 ± 0.2	33.1	
GJ 1111	08 29 49.34	+26 46 33.7	R	10 s	108	2010.16–2019.10	8.94	7	275.32 ± 1.39	1.27 ± 0.12	276.59 ± 1.40	1265.9 ± 0.50	242.0 ± 0.0	21.7	
GJ 2069 BD	08 31 37.58	+19 23 39.4	V	15 s	179	2003.95–2018.14	14.19	11	61.78 ± 2.50	0.68 ± 0.06	62.46 ± 2.50	248.0 ± 0.50	243.3 ± 0.2	18.8	
GJ 2069 ACE	08 31 37.58	+19 23 39.4	V	15 s	179	2003.95–2018.14	14.19	11	63.20 ± 1.85	0.68 ± 0.06	63.88 ± 1.85	252.9 ± 0.40	243.3 ± 0.2	18.8	
GJ 0317	08 40 59.21	−23 27 22.6	R	10 c	127	2009.04–2017.92	8.88	11	64.69 ± 1.07	1.50 ± 0.50	66.19 ± 1.18	928.3 ± 0.40	330.5 ± 0.1	64.8	Update
LEP 0844−4805	08 44 38.88	−49 20 26.2	R	5 c	82	2014.93–2019.09	4.16	12	72.00 ± 0.99	1.51 ± 0.23	73.51 ± 1.02	850.1 ± 0.60	339.1 ± 0.1	54.8	

Table 1
(Continued)

Name (1)	R.A. J2000.0 (2)	Decl. J2000.0 (3)	Filter (4)	$N_{\rm sea}$ (5)	$N_{\rm frm}$ (6)	Coverage (7)	Time (yr) (8)	$N_{\rm ref}$ (9)	$\pi_{\rm rel}$ (mas) (10)	$\pi_{\rm corr}$ (mas) (11)	$\pi_{\rm abs}$ (mas) (12)	μ (mas yr^{-1}) (13)	θ (deg) (14)	$V_{\rm tan}$ (km s^{-1}) (15)	Notes (16)
LEHPM2–0870	08 48 59.12	−80 35 01.7	I	5 c	75	2015.95–2020.16	4.21	10	41.88 ± 1.20	1.19 ± 0.09	43.07 ± 1.20	315.3 ± 0.70	211.6 ± 0.2	34.7	
2MA 0854–0551 AB	08 54 31.96	−05 51 25.8	I	6 c	84	2014.94–2020.16	5.22	9	43.19 ± 1.76	0.91 ± 0.09	44.10 ± 1.76	121.8 ± 1.00	249.1 ± 0.8	13.1	
LTT 12366 AB	09 01 10.49	+01 56 35.0	V	4 c	77	2014.92–2018.15	3.23	6	45.07 ± 1.61	1.84 ± 0.22	46.91 ± 1.62	389.5 ± 1.50	256.5 ± 0.4	39.4	
UPM 0901–6526	09 01 31.72	−65 26 40.3	V	7 s	76	2013.93–2019.93	6.00	11	54.94 ± 1.02	1.27 ± 0.09	56.21 ± 1.02	210.5 ± 0.50	343.2 ± 0.3	17.8	
LP 846–015	09 34 27.94	−26 43 26.8	R	5 s	63	2015.08–2019.36	4.27	9	70.15 ± 0.90	1.52 ± 0.10	71.67 ± 0.91	296.9 ± 0.50	94.0 ± 0.2	19.6	
GJ 0357	09 36 01.63	−21 39 38.8	V	11 s	122	2004.99–2019.35	14.36	10	104.30 ± 2.14	0.97 ± 0.18	105.27 ± 2.15	999.6 ± 0.40	171.5 ± 0.0	45.0	
GJ 0358	09 39 46.36	−41 04 03.3	V	11 s	111	2004.99–2019.10	14.11	7	102.04 ± 2.51	1.99 ± 0.15	104.03 ± 2.51	635.0 ± 0.40	304.4 ± 0.1	28.9	
WT 0244 AB	09 44 23.73	−73 58 38.3	I	8 s	69	1999.92–2019.93	20.01	10	45.46 ± 1.54	1.25 ± 0.23	46.71 ± 1.56	522.0 ± 0.30	258.2 ± 0.0	53.0	Update
GJ 0367	09 44 29.83	−45 46 35.6	V	15 s	151	2004.99–2019.34	14.35	7	104.64 ± 1.01	1.50 ± 0.50	106.14 ± 1.13	739.1 ± 0.20	218.5 ± 0.0	31.5	
G161–071	09 44 54.18	−12 20 54.4	V	11 s	100	2003.94–2019.35	15.41	9	74.93 ± 0.93	1.23 ± 0.16	76.16 ± 0.94	325.9 ± 0.20	277.4 ± 0.1	20.3	Update, PB
LP 728–071	09 52 41.77	−15 36 13.7	V	5 c	68	2014.06–2018.14	4.08	8	56.44 ± 0.95	0.97 ± 0.06	57.41 ± 0.95	174.0 ± 0.70	217.8 ± 0.5	14.4	
LP 847–048	09 55 23.86	−27 15 40.7	V	7 s	76	2013.27–2019.36	6.08	8	92.06 ± 1.87	0.62 ± 0.09	92.68 ± 1.87	185.9 ± 1.00	211.3 ± 0.6	9.5	
GJ 0375 AB	09 58 34.33	−46 25 30.4	V	7 c	91	2013.12–2019.35	6.23	10	63.65 ± 1.50	2.19 ± 0.34	65.84 ± 1.54	682.7 ± 0.70	134.5 ± 0.1	49.1	
LHS 0281	10 14 51.77	−47 09 24.1	R	12 s	130	2001.14–2019.35	18.20	10	79.39 ± 0.87	0.62 ± 0.03	80.01 ± 0.87	1126.5 ± 0.10	291.6 ± 0.0	66.7	Update
LP 790–002 A	10 18 13.86	−20 28 41.3	I	12 s	162	2005.09–2016.04	10.95	7	37.96 ± 1.09	1.56 ± 0.13	39.52 ± 1.10	383.4 ± 0.40	288.2 ± 0.1	46.0	
LP 790–002 B	10 18 13.86	−20 28 41.3	I	12 s	162	2005.09–2016.04	10.95	7	39.12 ± 1.03	1.56 ± 0.13	40.68 ± 1.04	377.9 ± 0.30	288.8 ± 0.1	44.0	
LP 848–050 AB	10 42 41.36	−24 16 04.9	R	8 s	93	2010.16–2017.36	7.20	13	90.97 ± 1.18	0.49 ± 0.05	91.46 ± 1.18	204.5 ± 0.40	13.5 ± 0.2	10.6	Update, PB
WT 1827 AB	10 43 02.81	−09 12 40.8	V	15 s	136	2000.06–2018.15	18.08	8	66.19 ± 1.30	0.52 ± 0.10	66.71 ± 1.30	1950.1 ± 0.20	280.2 ± 0.0	138.6	Update, PB
LHS 2310	10 47 38.69	−79 27 45.9	V	7 s	68	2013.11–2019.34	6.23	9	71.38 ± 1.31	1.59 ± 0.28	72.97 ± 1.34	484.5 ± 0.70	245.1 ± 0.1	31.5	
SDS 1048+0111	10 48 42.81	+01 11 58.1	I	8 s	29	2009.31–2016.19	6.88	7	71.03 ± 1.90	0.34 ± 0.16	71.37 ± 1.91	488.6 ± 0.80	243.1 ± 0.2	32.4	
GJ 0402	10 50 52.02	+06 48 29.4	V	11 s	80	2010.39–2020.14	9.75	7	144.00 ± 2.45	1.68 ± 0.43	145.68 ± 2.49	1177.1 ± 0.70	226.8 ± 0.1	38.3	
SIP 1054–8505	10 54 11.03	−85 05 02.3	I	8 s	47	2010.19–2019.10	8.91	8	53.24 ± 1.55	1.09 ± 0.06	54.33 ± 1.55	503.7 ± 0.50	305.0 ± 0.1	43.9	
LTT 04004 AB	10 54 41.97	−07 18 33.1	V	8 s	74	2013.12–2020.14	7.03	6	41.51 ± 1.66	0.87 ± 0.19	42.38 ± 1.67	408.6 ± 0.60	203.7 ± 0.2	45.7	Update, PB
LP 731–076	10 58 27.99	−10 46 30.5	I	15 s	121	2004.43–2019.10	14.66	5	65.28 ± 1.24	2.89 ± 0.76	68.17 ± 1.45	212.1 ± 0.20	247.0 ± 0.1	14.7	Update
UPM 1104–6232	11 04 33.80	−62 32 34.5	I	9 s	61	2011.16–2020.15	8.99	9	58.36 ± 1.49	1.73 ± 0.44	60.09 ± 1.55	224.9 ± 0.50	255.0 ± 0.2	17.7	
LHS 2397A AB	11 21 49.19	−13 13 08.5	I	12 s	113	2005.09–2018.15	13.05	9	67.31 ± 0.89	0.55 ± 0.07	67.86 ± 0.89	490.0 ± 0.20	265.5 ± 0.0	34.2	Update, PB
LP 672–042	11 30 41.82	−08 05 42.8	V	7 s	64	2013.12–2019.10	5.98	7	78.83 ± 1.98	1.29 ± 0.15	80.12 ± 1.99	442.4 ± 0.90	307.1 ± 0.2	26.2	PB
GJ 0431	11 31 46.51	−41 02 47.2	V	7 s	63	2013.12–2019.36	6.24	9	94.75 ± 2.07	2.48 ± 0.23	97.23 ± 2.08	722.4 ± 1.00	284.4 ± 0.1	35.2	
GJ 1156	12 18 59.41	+11 07 33.9	V	11 s	80	2010.39–2020.14	9.76	7	154.35 ± 1.33	0.91 ± 0.10	155.26 ± 1.33	1285.2 ± 0.40	279.9 ± 0.0	39.2	
2MA 1221+0257	12 21 27.71	+02 57 19.9	I	8 s	33	2009.32–2016.19	6.87	7	54.51 ± 1.95	0.52 ± 0.03	55.03 ± 1.95	138.4 ± 0.50	251.1 ± 0.4	11.9	
GJ 0465	12 24 52.49	−18 14 32.3	V	19 s	188	2000.14–2019.48	19.34	5	112.69 ± 1.26	1.88 ± 0.28	114.57 ± 1.29	2553.2 ± 0.20	154.6 ± 0.0	105.6	Update
LHS 2557	12 25 32.02	−15 59 41.8	R	7 s	73	2002.29–2019.34	17.05	6	77.26 ± 0.87	0.47 ± 0.05	77.73 ± 0.87	809.2 ± 0.40	272.2 ± 0.0	49.3	
LP 615–149 AB	12 27 44.70	−03 15 00.6	V	6 s	60	2013.11–2018.48	5.38	7	41.44 ± 2.72	0.64 ± 0.24	42.08 ± 2.73	285.5 ± 1.80	265.1 ± 0.5	32.2	
GJ 0469 AB	12 28 57.60	+08 25 31.7	V	17 s	167	2002.23–2019.49	17.26	6	71.75 ± 1.20	1.15 ± 0.08	72.90 ± 1.20	686.1 ± 0.20	246.2 ± 0.0	44.6	PB
GJ 0479	12 37 52.24	−52 00 05.5	V	11 s	99	2005.10–2019.49	14.39	9	104.82 ± 1.29	2.84 ± 0.23	107.66 ± 1.31	1024.6 ± 0.30	271.0 ± 0.0	45.1	
GJ 0480.1	12 40 46.28	−43 33 59.1	V	13 s	78	2003.51–2019.35	15.84	12	125.50 ± 1.16	1.83 ± 0.26	127.33 ± 1.19	1032.8 ± 0.20	311.7 ± 0.0	38.4	
GJ 0486	12 47 56.66	+09 45 05.1	V	11 s	103	2010.39–2020.16	9.77	8	120.25 ± 2.20	2.17 ± 0.57	122.42 ± 2.27	1095.6 ± 0.60	245.1 ± 0.1	42.4	
LEHPM2–0174	12 50 52.65	−21 21 13.6	I	12 s	86	2005.14–2017.37	12.23	6	54.99 ± 0.89	0.44 ± 0.03	55.43 ± 0.89	568.1 ± 0.20	125.4 ± 0.0	48.6	Update, PB
2MA 1300+1912	13 00 42.51	+19 12 34.5	I	7 c	55	2009.09–2015.42	6.33	7	70.90 ± 2.03	0.64 ± 0.04	71.54 ± 2.03	1474.7 ± 1.00	212.8 ± 0.1	97.7	
L257–129	13 22 04.74	−55 00 59.1	V	5 c	60	2015.21–2019.34	4.13	12	67.39 ± 1.02	1.90 ± 0.20	69.29 ± 1.04	293.1 ± 0.90	242.7 ± 0.3	20.1	
G014–052 AB	13 24 46.48	−05 04 19.7	V	8 s	83	2010.40–2019.50	9.10	8	43.02 ± 2.16	0.81 ± 0.15	43.83 ± 2.17	306.8 ± 0.90	166.5 ± 0.3	33.2	
LHS 2758	13 34 23.61	−26 22 11.8	R	5 c	60	2015.22–2019.11	3.89	8	40.85 ± 0.96	0.85 ± 0.10	41.70 ± 0.97	781.4 ± 0.80	242.7 ± 0.1	88.8	
LHS 2794	13 45 50.71	−17 58 05.7	V	7 s	76	2013.25–2019.35	6.10	8	89.33 ± 1.79	0.64 ± 0.12	89.97 ± 1.79	628.6 ± 0.80	207.9 ± 0.1	33.1	
LP 911–056	13 46 46.04	−31 49 25.6	I	7 s	91	2014.45–2020.15	5.70	13	73.00 ± 0.97	0.48 ± 0.04	73.48 ± 0.97	368.9 ± 0.60	295.0 ± 0.2	23.8	
LP 739–003	13 58 19.60	−13 16 24.9	R	6 c	80	2014.17–2019.47	5.31	8	64.10 ± 1.60	0.51 ± 0.05	64.61 ± 1.60	357.0 ± 0.90	99.8 ± 0.2	26.2	
LHS 2848	14 02 28.88	−21 00 36.8	R	5 c	59	2014.17–2018.49	4.32	8	50.52 ± 1.69	1.39 ± 0.19	51.91 ± 1.70	627.1 ± 1.30	127.7 ± 0.2	57.3	

Table 1
(Continued)

Name (1)	R.A. J2000.0 (2)	Decl. J2000.0 (3)	Filter (4)	$N_{\rm sea}$ (5)	$N_{\rm frm}$ (6)	Coverage (7)	Time (yr) (8)	$N_{\rm ref}$ (9)	$\pi_{\rm rel}$ (mas) (10)	$\pi_{\rm corr}$ (mas) (11)	$\pi_{\rm abs}$ (mas) (12)	μ (mas yr^{-1}) (13)	θ (deg) (14)	$V_{\rm tan}$ (km s^{-1}) (15)	Notes (16)
GJ 1183 B	14 27 56.08	−00 22 31.1	V	8 s	70	2013.25–2020.16	6.91	10	56.47 ± 0.92	1.06 ± 0.10	57.53 ± 0.93	357.0 ± 0.50	280.1 ± 0.1	29.4	
GJ 1183 A	14 27 56.08	−00 22 31.1	V	8 s	70	2013.25–2020.16	6.91	10	57.23 ± 0.93	1.08 ± 0.08	58.31 ± 0.93	353.9 ± 0.50	278.4 ± 0.1	28.8	
GJ 0553.1	14 31 01.15	−12 17 45.9	V	7 c	90	2013.26–2019.50	6.24	9	93.09 ± 1.93	0.96 ± 0.18	94.05 ± 1.94	561.9 ± 1.00	225.5 ± 0.2	28.3	
DEN 1454−6604 AB	14 54 07.96	−66 04 47.6	I	11 s	69	2009.32–2019.34	10.02	15	91.28 ± 1.14	0.70 ± 0.19	91.98 ± 1.16	587.9 ± 0.40	125.1 ± 0.1	30.3	Update, PB
L072−010	15 02 07.67	−71 18 01.3	V	6 c	77	2013.25–2019.47	6.22	11	50.45 ± 0.85	1.53 ± 0.13	51.98 ± 0.86	329.0 ± 0.50	225.0 ± 0.2	30.0	
LHS 3045	15 14 54.39	−31 50 13.6	R	5 s	66	2006.30–2011.70	5.40	8	11.87 ± 0.80	2.38 ± 0.29	14.25 ± 0.85	930.3 ± 0.50	216.9 ± 0.1	309.5	Update
GJ 0590	15 36 34.49	−37 54 22.8	V	4 s	45	2013.38–2016.21	2.83	10	98.97 ± 1.14	1.38 ± 0.17	100.35 ± 1.15	857.2 ± 1.10	202.6 ± 0.1	40.5	
GJ 0592	15 36 58.63	−14 08 01.7	V	7 s	69	2013.38–2019.36	5.97	9	71.06 ± 1.14	0.97 ± 0.18	72.03 ± 1.15	767.4 ± 0.70	215.5 ± 0.1	50.5	
SCR 1546−5534 AB	15 46 41.84	−55 34 47.0	I	10 c	151	2011.50–2020.15	8.65	9	92.65 ± 1.73	1.50 ± 0.50	94.15 ± 1.80	432.0 ± 0.70	229.4 ± 0.2	21.3	PB
LP 553−044 AB	16 01 56.47	−33 57 07.4	V	5 s	76	2015.41–2019.62	4.21	9	64.04 ± 0.92	2.72 ± 0.26	66.76 ± 0.96	429.1 ± 0.50	227.5 ± 0.1	30.5	
GJ 0609	16 02 50.94	+20 35 21.1	V	7 c	80	2010.40–2017.53	7.13	8	100.58 ± 1.71	2.08 ± 0.36	102.66 ± 1.75	1559.3 ± 0.90	217.8 ± 0.1	72.0	
LP 805−001	16 20 41.86	−20 05 14.0	V	6 s	61	2013.26–2019.63	6.37	5	36.78 ± 4.00	1.50 ± 0.50	38.28 ± 4.03	176.6 ± 1.60	235.6 ± 1.0	20.8	
GJ 0628	16 30 18.07	−12 39 45.4	V	12 s	153	2003.51–2014.44	10.93	5	228.96 ± 2.26	1.50 ± 0.50	230.31 ± 2.31	1191.6 ± 0.70	185.4 ± 0.1	23.4	Update
LHS 0423	16 35 40.40	−30 51 20.2	V	3 c	51	2001.43–2004.44	3.01	12	47.73 ± 1.39	2.04 ± 0.23	49.77 ± 1.41	1157.6 ± 0.90	223.4 ± 0.1	110.3	Update
GJ 2122 AB	16 45 16.97	−38 48 33.3	V	20 s	264	2000.58–2020.14	19.57	6	73.18 ± 2.04	1.50 ± 0.50	74.68 ± 2.10	55.1 ± 0.40	196.8 ± 0.7	3.3	PB
GJ 0643	16 55 25.23	−08 19 21.4	V	16 s	157	2003.52–2018.48	14.96	8	152.59 ± 1.23	1.50 ± 0.50	154.09 ± 1.33	1206.6 ± 0.30	223.4 ± 0.0	36.7	
GJ 0644 C	16 55 35.25	−08 23 40.7	I	14 s	211	2001.53–2014.43	12.90	7	153.42 ± 0.47	2.01 ± 0.14	155.43 ± 0.49	1188.3 ± 0.20	224.0 ± 0.0	36.2	
UPM 1710−5300 AB	17 10 44.31	−53 00 25.1	V	7 s	62	2010.50–2018.49	7.99	11	55.73 ± 2.04	2.67 ± 0.31	58.40 ± 2.06	161.3 ± 0.70	190.9 ± 0.4	13.1	Update, PB
SIP 1712−0323	17 12 04.36	−03 23 29.9	I	8 s	60	2009.54–2019.35	9.81	12	51.57 ± 0.86	1.14 ± 0.12	52.71 ± 0.87	409.7 ± 0.40	244.2 ± 0.1	36.8	
GJ 1215 AB	17 17 44.09	+11 40 11.9	I	17 s	263	2002.46–2018.48	16.02	8	78.74 ± 0.68	0.99 ± 0.08	79.73 ± 0.68	534.7 ± 0.10	219.7 ± 0.0	31.8	Orbit
LHS 0440	17 18 25.58	−43 26 37.6	R	16 s	216	2000.58–2019.64	19.06	9	34.36 ± 0.80	1.85 ± 0.52	36.21 ± 0.95	1077.7 ± 0.10	232.9 ± 0.0	141.1	Update, PB
GJ 0680 AB	17 35 13.62	−48 40 51.2	V	17 s	186	2003.52–2019.61	16.09	7	105.00 ± 1.17	2.06 ± 0.14	107.06 ± 1.18	478.3 ± 0.20	8.5 ± 0.1	21.2	PB
GJ 0682	17 37 03.65	−44 19 09.2	V	15 s	212	2003.52–2017.48	13.96	8	201.99 ± 1.20	1.50 ± 0.50	203.49 ± 1.30	1165.1 ± 0.30	217.2 ± 0.0	26.7	PB
GJ 2130 A	17 46 12.75	−32 06 09.3	V	6 s	77	1999.64–2019.34	19.71	7	71.34 ± 1.39	2.61 ± 0.74	73.95 ± 1.57	276.2 ± 0.30	195.7 ± 0.1	17.7	Update
GJ 2130 BC	17 46 14.42	−32 06 08.5	V	6 s	122	1999.64–2019.34	19.71	7	70.20 ± 1.03	2.61 ± 0.74	72.81 ± 1.27	276.9 ± 0.20	195.8 ± 0.1	18.0	Update
GJ 0693	17 46 34.22	−57 19 08.7	V	13 s	116	2003.51–2019.64	16.13	11	168.58 ± 1.48	1.50 ± 0.50	170.08 ± 1.56	1744.0 ± 0.30	219.4 ± 0.0	47.7	PB
DEN 1756−4805	17 56 56.20	−48 05 09.7	I	11 s	41	2009.32–2019.64	10.32	9	48.92 ± 0.79	0.73 ± 0.09	49.65 ± 0.80	84.7 ± 0.20	66.9 ± 0.3	8.1	Orbit
G154−043 AB	18 03 36.07	−18 58 50.5	R	8 s	103	2010.20–2019.64	9.44	8	72.26 ± 0.71	1.50 ± 0.50	73.76 ± 0.87	351.5 ± 0.20	154.0 ± 0.1	22.1	Update, PB
G182−041 AB	18 09 26.55	+27 55 23.3	R	5 c	53	2007.44–2011.62	4.18	8	8.37 ± 2.24	1.11 ± 0.13	9.48 ± 2.24	278.1 ± 2.00	240.8 ± 0.8	139.1	Update, orbit
SCR 1848−6855 AB	18 48 21.01	−68 55 34.1	I	15 s	211	2003.24–2017.72	14.48	11	37.19 ± 1.03	1.11 ± 0.08	38.30 ± 1.03	1269.9 ± 0.20	195.7 ± 0.0	157.1	Update, PB
LP 691−015	18 49 06.41	−03 15 17.5	R	10 s	76	2010.50–2019.34	8.84	9	58.56 ± 0.93	1.50 ± 0.50	60.06 ± 1.06	267.6 ± 0.30	91.3 ± 0.1	18.3	Update
GJ 0732	18 53 39.92	−38 36 44.5	V	7 s	63	2013.38–2019.49	6.11	9	79.30 ± 0.94	0.59 ± 0.04	79.89 ± 0.94	983.2 ± 0.40	158.1 ± 0.0	58.3	
GJ 0752 B	19 16 57.61	+05 09 01.6	I	11 s	87	2009.56–2019.49	9.93	5	167.40 ± 0.91	2.10 ± 0.49	169.50 ± 1.03	1481.7 ± 0.30	203.6 ± 0.0	41.4	
GJ 0754	19 20 47.98	−45 33 29.7	V	21 s	287	1999.64–2019.34	19.71	12	168.18 ± 0.88	0.40 ± 0.00	168.58 ± 0.88	2959.9 ± 0.20	168.0 ± 0.0	83.2	Update, PB
LHS 0475	19 20 54.26	−82 33 16.1	V	14 s	124	2000.57–2019.61	19.04	7	78.59 ± 0.91	1.36 ± 0.08	79.95 ± 0.91	1269.0 ± 0.10	164.8 ± 0.0	75.2	Update
GJ 1235	19 21 38.70	+20 52 03.2	R	10 s	91	2010.50–2019.34	8.84	7	94.74 ± 1.21	1.50 ± 0.50	96.24 ± 1.31	1733.7 ± 0.40	213.7 ± 0.0	83.1	Update
2MA 1943−3722 AB	19 43 24.67	−37 22 11.1	V	4 c	57	2016.63–2019.77	3.15	10	42.04 ± 1.07	0.49 ± 0.04	42.53 ± 1.07	238.6 ± 0.80	137.5 ± 0.4	26.6	
2MA 1951−3510 B	19 51 35.89	−35 10 37.5	V	7 s	78	2010.73–2016.74	6.01	10	81.39 ± 2.00	1.50 ± 0.50	82.89 ± 2.06	359.3 ± 1.00	81.2 ± 0.3	20.1	
2MA 1951−3510 A	19 51 35.89	−35 10 37.5	V	7 s	78	2010.73–2016.74	6.01	10	100.78 ± 1.89	1.50 ± 0.50	102.28 ± 1.96	393.3 ± 1.00	73.5 ± 0.2	17.9	
UPM 1951−3100 AB	19 51 40.42	−31 00 21.8	V	5 c	81	2015.39–2019.74	4.35	8	75.63 ± 1.36	0.46 ± 0.06	76.09 ± 1.36	147.0 ± 0.80	166.2 ± 0.6	9.2	PB
LP 754−008	19 57 51.97	−10 53 05.4	R	6 sa	67	2014.67–2019.63	4.96	9	40.43 ± 0.94	1.54 ± 0.11	41.97 ± 0.95	479.5 ± 0.50	234.3 ± 0.1	54.2	
LHS 3514	20 03 58.90	−08 07 47.4	V	7 s	61	2013.53–2019.35	5.82	11	52.27 ± 1.34	1.42 ± 0.17	53.69 ± 1.35	555.9 ± 0.70	245.0 ± 0.1	49.1	
LEHPM2−0064	20 07 55.24	−42 05 14.7	V	7 s	71	2013.53–2019.77	6.23	8	64.46 ± 0.92	1.90 ± 0.17	66.36 ± 0.94	744.6 ± 0.40	176.4 ± 0.1	53.2	
LTT 07967	20 09 51.61	−47 31 34.3	R	5 s	61	2015.56–2019.61	4.05	14	52.83 ± 1.07	1.00 ± 0.13	53.83 ± 1.08	338.0 ± 0.60	177.4 ± 0.2	29.8	
L209−071 ABC	20 15 22.67	−56 45 54.2	R	7 c	84	2013.38–2019.63	6.25	11	39.78 ± 1.25	1.25 ± 0.17	41.03 ± 1.26	334.1 ± 0.50	187.7 ± 0.1	38.6	PB
LP 927−008	20 20 43.60	−28 06 06.6	V	9 s	66	2008.71–2019.49	10.78	7	42.76 ± 1.07	1.25 ± 0.07	44.01 ± 1.07	212.7 ± 0.40	287.3 ± 0.2	22.9	

Table 1
(Continued)

Name (1)	R.A. J2000.0 (2)	Decl. J2000.0 (3)	Filter (4)	N_{sea} (5)	N_{frm} (6)	Coverage (7)	Time (yr) (8)	N_{ref} (9)	π_{rel} (mas) (10)	π_{corr} (mas) (11)	π_{abs} (mas) (12)	μ (mas yr^{-1}) (13)	θ (deg) (14)	V_{tan} (km s^{-1}) (15)	Notes (16)
GJ 0791.2 AB	20 29 48.32	+09 41 20.2	I	14 s	198	2004.33–2017.52	13.19	7	111.40 ± 1.52	2.71 ± 0.17	114.11 ± 1.53	685.0 ± 0.40	80.6 ± 0.1	28.5	PB
GJ 1256	20 40 33.87	+15 29 58.9	R	10 s	97	2010.50–2019.77	9.27	12	104.62 ± 1.05	1.91 ± 0.16	106.53 ± 1.06	1482.2 ± 0.40	63.5 ± 0.0	65.9	
SIP 2045–6332	20 45 02.38	−63 32 06.6	I	8 s	93	2010.59–2017.53	6.94	9	45.17 ± 1.07	1.07 ± 0.07	46.24 ± 1.07	223.9 ± 0.50	157.1 ± 0.2	23.0	Update, PB
LHS 0501 AC	20 55 37.76	−14 02 08.1	V	14 s	158	1999.71–2019.74	20.04	9	76.68 ± 0.91	0.88 ± 0.05	77.56 ± 0.91	1488.3 ± 0.10	107.9 ± 0.0	91.0	Update, PB
2MA 2057–0252	20 57 54.09	−02 52 30.4	I	10 s	53	2010.50–2019.76	9.26	12	61.09 ± 0.96	0.94 ± 0.10	62.03 ± 0.97	91.1 ± 0.30	179.4 ± 0.2	7.0	
WT 0766 AC	21 01 07.41	−49 07 24.9	R	9 c	111	2010.40–2018.73	8.33	11	75.59 ± 0.80	0.66 ± 0.06	76.25 ± 0.80	364.9 ± 0.30	234.9 ± 0.1	22.7	Update, orbit
GJ 2151	21 03 13.94	−56 57 48.3	V	7 s	70	2013.52–2019.63	6.11	12	78.04 ± 1.26	1.04 ± 0.17	79.08 ± 1.27	511.5 ± 0.60	315.3 ± 0.1	30.7	
2MA 2104–1037	21 04 14.96	−10 37 37.4	I	9 s	47	2009.56–2017.52	7.96	10	57.43 ± 0.98	0.77 ± 0.15	58.20 ± 0.99	663.9 ± 0.30	115.9 ± 0.1	54.1	Update, PB
LHS 0510	21 30 47.67	−40 42 29.5	R	11 s	138	2000.57–2018.77	18.19	6	78.95 ± 0.92	1.76 ± 0.18	80.71 ± 0.94	1724.4 ± 0.20	143.0 ± 0.0	101.3	Update, PB
GJ 0831 AB	21 31 18.64	−09 47 26.4	V	15 s	255	2003.52–2017.82	14.30	6	127.42 ± 1.11	1.84 ± 0.18	129.26 ± 1.12	1182.5 ± 0.30	92.5 ± 0.0	43.4	PB
WT 0792	21 34 22.29	−43 16 10.6	I	7 c	104	2012.88–2019.61	6.73	8	59.66 ± 0.66	0.58 ± 0.04	60.24 ± 0.66	798.0 ± 0.40	170.0 ± 0.0	62.8	PB
LHS 0512	21 38 43.65	−33 39 55.3	V	11 s	117	2000.57–2018.68	18.11	7	80.58 ± 0.93	1.13 ± 0.04	81.71 ± 0.93	1153.9 ± 0.10	116.5 ± 0.0	66.9	Update, PB
GJ 0836 AB	21 39 00.92	−24 09 29.0	V	7 s	70	2013.53–2019.64	6.11	9	54.11 ± 1.29	0.64 ± 0.12	54.75 ± 1.30	1220.3 ± 0.60	125.0 ± 0.1	105.7	PB
WT 0818 AB	21 49 44.81	−41 38 32.8	R	7 s	72	2013.52–2019.63	6.11	8	45.27 ± 1.59	0.60 ± 0.06	45.87 ± 1.59	179.0 ± 0.80	102.9 ± 0.4	18.5	PB
LHS 0516	21 56 55.25	−01 54 09.3	R	7 s	60	2013.53–2019.50	5.97	13	74.47 ± 1.46	0.62 ± 0.12	75.09 ± 1.46	1419.3 ± 0.70	64.1 ± 0.1	89.6	
LHS 3739 A	21 58 49.13	−32 26 25.5	R	17 s	211	1999.64–2017.72	18.08	11	51.52 ± 0.69	1.40 ± 0.21	52.92 ± 0.72	535.9 ± 0.10	229.0 ± 0.0	48.0	Update, orbit
G188–038	22 01 13.11	+28 18 24.9	V	4 c	55	2009.56–2014.81	5.25	8	108.24 ± 2.38	1.24 ± 0.18	109.48 ± 2.39	376.2 ± 1.50	84.0 ± 0.3	16.3	
GJ 0845 BC	22 04 10.59	−56 46 58.1	I	15 s	102	2004.58–2019.51	14.93	10	277.22 ± 1.73	0.79 ± 0.05	278.01 ± 1.73	4697.7 ± 0.50	122.2 ± 0.0	80.1	Orbit
GJ 1265	22 13 42.87	−17 41 08.7	R	7 s	63	2013.66–2019.77	6.11	9	95.89 ± 1.09	0.75 ± 0.03	96.64 ± 1.09	907.7 ± 0.50	109.4 ± 0.1	44.5	
SCR 2216–4800	22 16 40.65	−48 00 36.3	V	7 s	55	2013.53–2019.49	5.96	6	37.36 ± 1.20	1.20 ± 0.11	38.56 ± 1.21	155.5 ± 0.60	355.4 ± 0.3	19.1	
LP 984–001	22 17 19.24	−34 44 03.4	R	6 s	63	2013.66–2018.68	5.03	9	46.94 ± 1.01	0.75 ± 0.11	47.69 ± 1.02	461.7 ± 0.60	167.0 ± 0.1	45.9	
LHS 3799	22 23 07.00	−17 36 26.1	V	11 s	129	2003.52–2018.72	15.20	6	139.75 ± 1.67	0.47 ± 0.14	140.22 ± 1.68	767.8 ± 0.20	157.5 ± 0.0	26.0	Update
LTT 09084	22 35 04.90	−42 17 48.1	R	7 s	66	2013.66–2019.52	5.86	5	42.54 ± 1.52	1.32 ± 0.21	43.86 ± 1.53	279.2 ± 0.70	120.7 ± 0.3	30.2	
GJ 0865 AB	22 38 29.76	−65 22 42.4	V	7 s	64	2013.67–2019.62	5.95	8	75.11 ± 1.43	1.22 ± 0.12	76.33 ± 1.44	828.1 ± 0.70	100.8 ± 0.1	51.4	
SCR 2303–4650 AB	23 03 35.61	−46 50 47.0	V	11 s	128	2009.63–2019.75	10.12	9	62.87 ± 0.99	0.56 ± 0.06	63.43 ± 0.99	191.9 ± 0.30	266.9 ± 0.1	14.3	Update, orbit
GJ 1281	23 10 42.16	−19 13 34.9	V	6 s	84	2000.57–2019.74	19.17	7	37.72 ± 1.58	0.98 ± 0.06	38.70 ± 1.58	1434.8 ± 0.20	178.6 ± 0.0	175.7	Update, PB
LHS 0539	23 15 51.61	−37 33 30.6	R	4 s	57	2000.87–2003.77	2.89	8	46.53 ± 1.00	0.92 ± 0.07	47.45 ± 1.00	1309.9 ± 1.50	77.7 ± 0.1	130.9	Update
SCR 2325–6740 AB	23 25 25.13	−67 40 07.9	R	8 s	66	2009.74–2019.77	10.03	8	30.63 ± 1.53	1.00 ± 0.10	31.63 ± 1.53	253.5 ± 0.60	121.6 ± 0.3	38.0	
LHS 0547	23 36 52.31	−36 28 51.8	V	12 s	120	2000.57–2018.68	18.11	6	82.27 ± 0.90	0.72 ± 0.04	82.99 ± 0.90	1169.1 ± 0.10	86.9 ± 0.0	66.8	Update, PB
LHS 4021	23 50 31.64	−09 33 32.6	V	11 s	104	2000.71–2019.74	19.04	4	58.07 ± 0.92	0.93 ± 0.04	59.00 ± 0.92	753.1 ± 0.10	122.3 ± 0.0	60.5	Update
2MA 2351–2537 AB	23 51 50.48	−25 37 36.7	I	11 s	100	2004.58–2017.72	13.14	9	49.07 ± 1.03	0.49 ± 0.04	49.56 ± 1.03	405.3 ± 0.30	61.4 ± 0.1	38.8	Update, PB
LHS 4058	23 59 51.38	−34 06 42.5	V	11 s	84	2000.41–2018.49	18.08	6	65.05 ± 0.98	1.99 ± 0.38	67.04 ± 1.05	940.8 ± 0.20	132.6 ± 0.0	66.5	Update

Note. Column 16 (Notes) indicates whether a result is an update to a previously published result for this system ("update") in the *Solar Neighborhood* series, a preliminary orbit has been fit to improve the astrometry ("orbit"), or the astrometry shows a perturbation that does not yet permit an orbit fit ("PB").

(This table is available in its entirety in machine-readable form.)

Table 2
Astrometric Solutions from RECONS and Gaia DR2 for Red Dwarfs within 25 pc Common to Both of These Catalogs

Name (1)	R.A. J2000.0 (2)	Decl. J2000.0 (3)	RECONS π_{abs} (mas) (4)	Ref. (5)	Gaia DR2 π_{abs} (mas) (6)	Goodness of Fit (7)	Excess Noise (8)	Excess Noise Sig. (9)	N_{good} (10)	N_{bad} (11)	N_{bad}/N_{good} (%) (12)	RUWE (13)	G (mag) (14)	Class. (15)	Sus. (16)
GJ 1001 BC	00 04 36.46	−40 44 02.7	77.02 ± 2.07	Die14	82.095 ± 0.377	14.161	1.460	15.3	271	5	1.8	1.176	18.35	unr	
GJ 1001 A	00 04 36.46	−40 44 02.7	81.76 ± 1.65	*	81.228 ± 0.114	40.520	0.285	45.4	253	13	5.1	1.409	11.50	res	
GJ 1002	00 06 43.19	−07 32 17.0	207.18 ± 3.09	Dav15	206.213 ± 0.128	51.302	0.366	63.8	261	5	1.9	1.280	11.78		
LTT 00057	00 08 17.37	−57 05 52.9	75.17 ± 2.11	Win17	78.115 ± 0.061	24.222	0.172	14.0	213	9	4.2	1.123	10.94		
G131–026 AB	00 08 53.92	+20 50 25.4	54.13 ± 1.35	Rie14	55.255 ± 0.761	333.638	4.059	6740.0	165	8	4.8	21.268	11.99	unr	✓
LEHPM 1–0255 AB	00 09 45.06	−42 01 39.6	57.03 ± 1.16	*	57.200 ± 0.245	121.537	0.996	516.0	343	59	17.2	3.749	12.15	unr	
GJ 1005 AB	00 15 28.07	−16 08 01.8	169.79 ± 2.67	*		247.417	8.177	16100.0	65	0	0.0		10.15	unr	✓
LHS 1050	00 15 49.25	+13 33 22.3	85.85 ± 2.57	Rie10	81.871 ± 0.087	24.271	0.187	15.0	150	7	4.7	1.220	11.40		
NLTT 01261	00 24 24.63	−01 58 20.0	82.43 ± 2.22	Rie18	79.965 ± 0.221	36.677	1.105	66.0	349	0	0.0	1.213	16.60		
GJ 2005 ABC	00 24 44.19	−27 08 24.2	117.71 ± 3.22	*		47.837	1.090	214.0	96	0	0.0		13.09	unr	✓

Note. Columns 7–14 reproduce the parameters characterizing the DR2 astrometric fits. Column 15 ("Class.") indicates the classification given to each system in the plots of Figures 4–6: res = resolved companion, unr = unresolved multiple, PB = perturbation in RECONS astrometric residuals (but companion not yet confirmed), no label = presumed single. Check marks in column 16 ("Sus.") indicate the systems that meet all four criteria given in Section 7.3 for suspicion of being unresolved multiples. Systems that are missing parallaxes in DR2 have been included in that set. Reference codes for RECONS parallaxes: * = this work, Bar17 = Bartlett et al. (2017), Ben16 = Benedict et al. (2016), Dav15 = Davison et al. (2015), Hen18 = Henry et al. (2018), Jao05 = Jao et al. (2005), Jao11 = Jao et al. (2011), Jao17 = Jao et al. (2017), Lur14 = Lurie et al. (2014), Rie10 = Riedel et al. (2010), Rie14 = Riedel et al. (2014), Rie18 = Riedel et al. (2018), Sub09 = Subasavage et al. (2009), Win17 = Winters et al. (2017).

(This table is available in its entirety in machine-readable form.)

astrometry targets were red and brown dwarfs that were deemed likely to be nearby but were missing precise trigonometric parallaxes. These targets were selected from proper-motion surveys and photometric distance measurements. After the RECONS program graduated from the NOAO surveys program, it continued fulfilling the spirit of that effort, providing a database of time-series astrometric and photometric observations that have been fundamental to investigations of several aspects of these nearby M stars beyond their distances. These studies, collected in the *Solar Neighborhood* series of papers, include work on M dwarf populations (Henry et al. 2006; Winters et al. 2017; Henry et al. 2018), ages (Riedel et al. 2010, 2014, 2018), metallicities (Jao et al. 2005, 2011, 2017), surface activity and long-term photometric variability (Hosey et al. 2015; Clements et al. 2017), and multiplicity (Winters et al. 2019), as well as white dwarfs (Subasavage et al. 2009, 2017), the stellar–substellar boundary (Dieterich et al. 2014), and exoplanet searches (Lurie et al. 2014).

4. Astrometry Observations and Reductions

The parallax results and orbits presented here come from the astrometric monitoring program at the CTIO/SMARTS 0.9 m telescope. In this section, we focus on the details and capabilities of those observations.

4.1. Observing Red Dwarfs at the CTIO/SMARTS 0.9 m Telescope

All RECONS astrometry is currently carried out at the CTIO/SMARTS 0.9 m telescope with the same camera and CCD setup used for that program since its inception in 1999. The CCD is a Tektronics 2048×2048 with 401 mas pixel^{-1}, with only the central quarter ($6\rlap{.}'8 \times 6\rlap{.}'8$) used for astrometry observations in order to minimize coma and other distortions. Observations for each target are taken in either the *V*, *R*, or *I* filter[7]; the only discontinuity in the use of these filters is the period from 2005 March to 2009 August when the Tek No. 2 filter, which had become cracked, was replaced by the effectively identical Tek No. 1 filter. The Tek No. 1 filter matched the Tek No. 2 filter photometrically to 1% but resulted in systematic offsets in the astrometry (see Subasavage et al. 2009 and Riedel et al. 2010 for details), so we returned the Tek No. 2 filter to service in 2009 August. Those offsets are now avoided in each astrometry reduction by choosing reference stars located near the target star on the CCD where possible or omitting the Tek No. 1 frames for systems that have a sufficient number of Tek No. 2 frames.

The specifics of the observations are given briefly here but also described in more detail in Jao et al. (2005) and Henry et al. (2006). Each target is placed on the CCD such that the number of useful reference stars is maximized (most fields have 5–10) and is observed in a single filter (*V*, *R*, or *I*) chosen to maximize the number of counts in that target star and reference stars. Each target is visited at least twice per year, with three to five frames taken at each visit, each within 120 minutes of the target's transit of the meridian to minimize the correction needed for differential color refraction (DCR). Exposure times vary from 30 to 300 s, with some exceptional systems requiring up to 900 s, and exposures are adjusted on the fly by the

observer to accommodate minute-by-minute variations in seeing and targets of different brightness in different filters.

The full observing list consists of ∼700 red, brown, and white dwarfs observed in four to six runs per year of 10–16 nights each run. Proper motions and parallaxes are considered reliable when the data span at least 2 yr and 60 frames and about 12 visits. Many targets remain on the observing list after this point for long-term astrometric and photometric studies.

4.2. Astrometry Reductions: Characterizing Proper Motion, Parallax, and Orbital Motion

Astrometry reductions are conducted as described in Jao et al. (2005), so only the basic steps are summarized here. All frames are first bias-subtracted and flat-fielded in IRAF using the bias frames and dome flat frames taken nightly prior to observations. Astrometric reductions then proceed for each system using all frames accumulated for it during the program as follows.

1. Reference stars and the target star are tagged and centroided in each frame using SExtractor (Bertin & Arnouts 1996).
2. A representative, high-quality "trail plate" is chosen, and that field is matched to the 2MASS catalog (Cutri et al. 2003; Skrutskie et al. 2006) to determine rotation and scaling for that frame.
3. Target and reference star positions in all frames are measured relative to that trail plate and corrected for DCR using the empirical relation determined for our specific program (described in Jao et al. 2005).
4. Using GaussFit (Jefferys et al. 1987), a least-squares optimization is performed to determine the plate constants for each frame and relative proper motions of the reference stars and science target star, under the assumption that the reference stars' proper motions sum to zero.
5. The above GaussFit optimization also determines the relative parallax of the science star. This value is then corrected to absolute parallax using the photometric distances of the reference stars.

The result of this process is proper-motion, parallax, tangential velocity, and time-series residuals of the proper motion and parallax fit for each tagged star in the field. For single stars, these residuals are flat, with no long- or short-term trends. Two dozen single stars, spread evenly across all hours of R.A., are monitored to evaluate trends in residuals and thus confirm the astrometric stability of the telescope and instruments. The median deviation in the nightly mean points for these "flatline" systems is 2.36 and 2.55 mas in R.A. and decl., respectively, after proper-motion and parallax fits. The median parallax error for systems in the 25 pc sample is 1.40 mas.

Unresolved multiple systems are detectable in our data by periodic motions of the system's photocenter superimposed on the parallax and proper motion, corresponding to the photocenter's orbit around the system's center of mass. In these cases, our usual method is to fit the proper motion and parallax using the pipeline described above, then fit the orbital motion left in the residuals using the algorithm of Hartkopf et al. (1989). This preliminary orbital motion is then subtracted from the residuals, and the proper motion and parallax are fit again to secure a more precise solution. The orbit fit in most of these cases does not represent the final photocentric orbit unless more

---

[7] Here and throughout the paper, *V*, *R*, and *I* refer specifically to the Johnson *V* and Kron–Cousins *R* and *I* filters, respectively.

than one cycle has been observed. More robust orbital results are possible using an updated algorithm from Dieterich et al. (2018) that fits the parallax, proper motion, and photocentric orbital motion simultaneously; hence, that is the procedure we have employed for the orbits presented in Section 6.

5. RECONS Parallax Results

The decades-long baseline of this astrometry program has allowed it to fill a unique niche in stellar astrophysics through both the astrometry and the photometry available in these data. In its first decade, the program focused on filling the paucity of nearby red dwarf parallaxes, improving the total number of stellar systems known to be within 10 pc by 15%. As the Gaia mission filled gaps in the 25 pc sample and promises to continue adding to and validating these parallaxes in future data releases, the RECONS astrometry program has shifted toward harnessing the strength of up to 20 yr of observations of these targets. These time-series observations have already opened doors for more comprehensive multiplicity surveys (Winters et al. 2019), analyses of which systems do not have low-mass companions (Lurie et al. 2014), and studies of multiyear photometric variability cycles on these typically active stars (Hosey et al. 2015).

It is with this focus on system characterization that we present the parallaxes for 210 systems in Table 1, which includes 146 new values and 64 updates to the RECONS catalog since the last publication in this series (Henry et al. 2018). The final column of Table 1 notes whether a preliminary orbit has been fit to this astrometry data to improve the results ("orbit") or the time-series astrometric residuals have a perturbation to which we have not fit an orbit ("PB"). In most of the PB cases, we have no reason to suspect that the perturbation is not astrophysical, but the signal shape is not yet well defined enough to permit an orbit fit. That column also notes whether this result is an update of a previously published parallax in this series ("update"), defined as a change in absolute parallax of more than 2.0 mas, parallax error improvement by a factor of 2 or more, or a parallax error that fell from above 3.0 mas to below 2.0 mas. For each system, Table 1 gives the name (column 1), R.A. and decl. (columns 2 and 3), filter of our observations (column 4), number of seasons (column 5) and frames (column 6) over which it has been observed, dates of time coverage (column 7), and duration of time coverage (column 8). Also listed is the number of reference stars used in the final astrometry reduction (column 9), relative parallax (column 10), correction to parallax based on reference star photometric distances (column 11), and final absolute parallax (column 12). The proper motion (column 13), position angle of proper motion (column 14), and tangential velocity (column 15) are also results of our parallax solutions.

6. RECONS Orbit Results

Orbital motions and fits of nine systems selected from RECONS astrometry are shown in Figures 1–3. For each system, the left panels show R.A. and decl. residuals plotted against time after proper motions and parallax have been determined and causative shifts removed; deviations from a flat line indicate orbital motion. In the right column, the orbits are shown on the plane of the sky. In both views, the points represent mean positions from typically five

observations in a night, and the best-fit orbit is the solid curve. Note that each orbit represents the motion of the photocenter, i.e., the center of light. The semimajor axis of this orbit, as a fraction of the relative orbit of star B around star A, is directly proportional to the mass of star B relative to the total system mass and inversely proportional to the flux of star B relative to star A,[8] following the prescription by van de Kamp (1967).

The orbits are the result of images processed with the usual RECONS pipeline, as described in Section 4.2, through the step where the target positions are measured relative to the sidereal frame and corrected for DCR (step 3 in Section 4.2). The orbit fits were then derived using a different method than those used in previous publications in the *Solar Neighborhood* series. Here we use the Markov Chain Monte Carlo (MCMC) algorithm of Dieterich et al. (2018), where a thorough description of the technique can be found. Briefly, a fit is made for proper motion, parallax, and the seven orbital elements simultaneously, resulting in astrometry that reliably attributes the three different motions of the photocenter. The relative positions, together with their observation epochs and parallax factors, are the input for the MCMC fitting code, which is typically run with 51 chains of 200,000 steps each to identify the most likely values for the 10 parameters (proper motion in R.A. and decl., parallax, and the seven orbital motion parameters). The code varies the parameters uniformly over given ranges, with step sizes set such that no one parameter's convergence dominates the others. For these systems, the input parameter ranges were initially set to broad uniform priors for all but the parallax, which was informed by the preliminary RECONS values. After this initial run, we fit each system again using narrower parameter ranges based on the results of the preliminary run. Convergence was judged by plotting the probability density functions based on the last 10,000 chains; Gaussian distributions indicate good convergence.

The orbital elements for each fit are given in Table 3. Figure 1 illustrates three systems used for calibration that have well-known orbits of short, medium, and long duration, demonstrating the capabilities of our fitting procedure over each of these timescales: GJ 748 AB ($P = 2.49$ yr), GJ 1005 AB (4.56 yr), and GJ 234 AB (16.63 yr). These three systems were observed using (primarily) interferometric measurements from a long-term Hubble Space Telescope Fine Guidance Sensors program, augmented with radial velocities from McDonald Observatory, as described in Benedict et al. (2016). Comparisons of the relative orbits in Benedict et al. (2016) to our orbits, both included in Table 3, indicate that most elements match to within the error bars for all expected, except the argument of periastron (ω) and longitude of the ascending node (Ω) for GJ 748 AB, which differ by 65°.2 and 17°.9, respectively. Note that for each calibration system, our semimajor axis (a) is not expected to match that of Benedict et al. (2016) because our data are for photocentric orbits rather than relative orbits, and Ω and ω will differ in quadrant by 180°.

Figures 2 and 3 illustrate six new orbits for red dwarf binaries within 25 pc. Several are updates from previous orbits in this series of papers; these new orbits are more reliable given the new technique of fitting for proper motion, parallax, and orbital motion simultaneously. We consider all six orbits to be

---

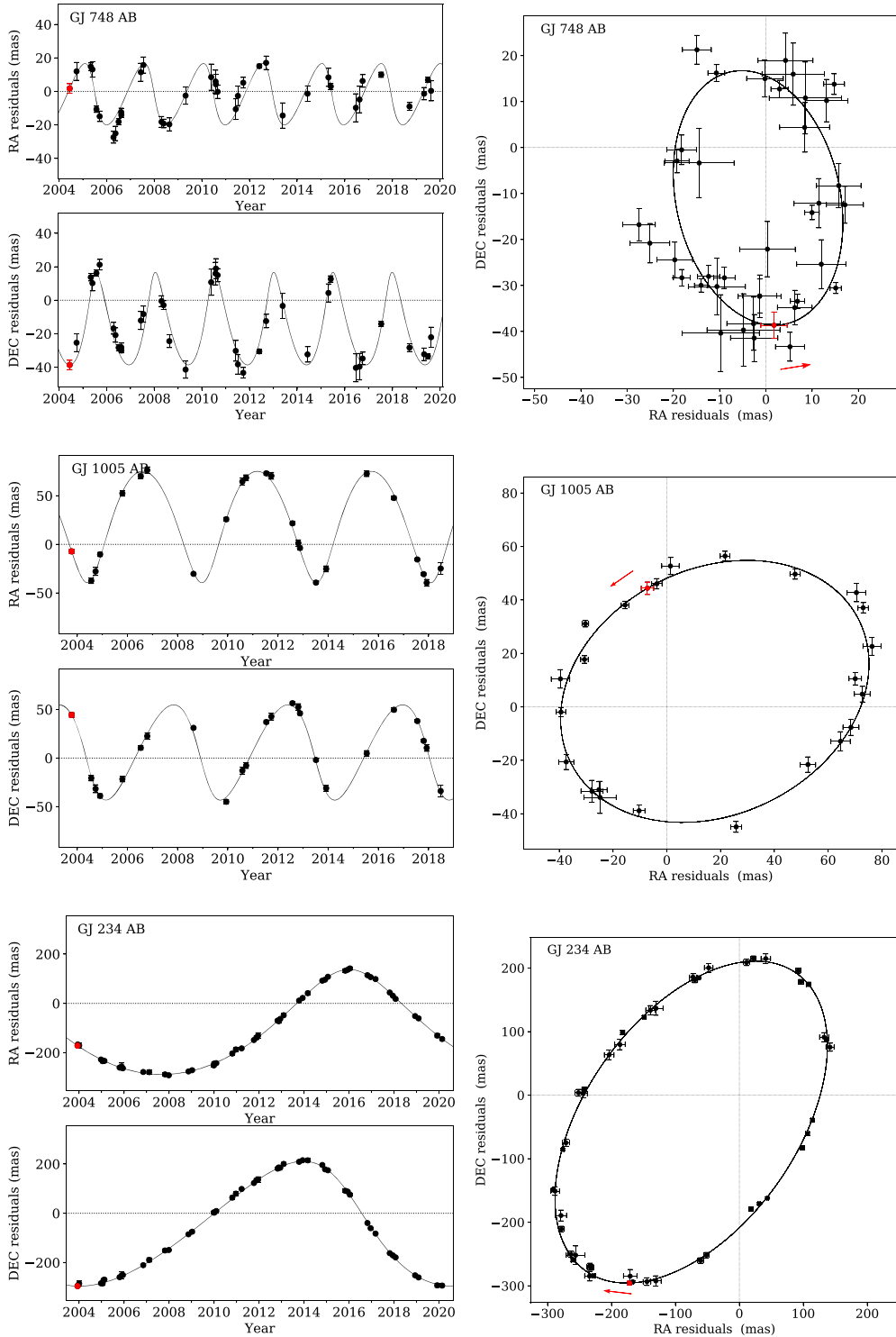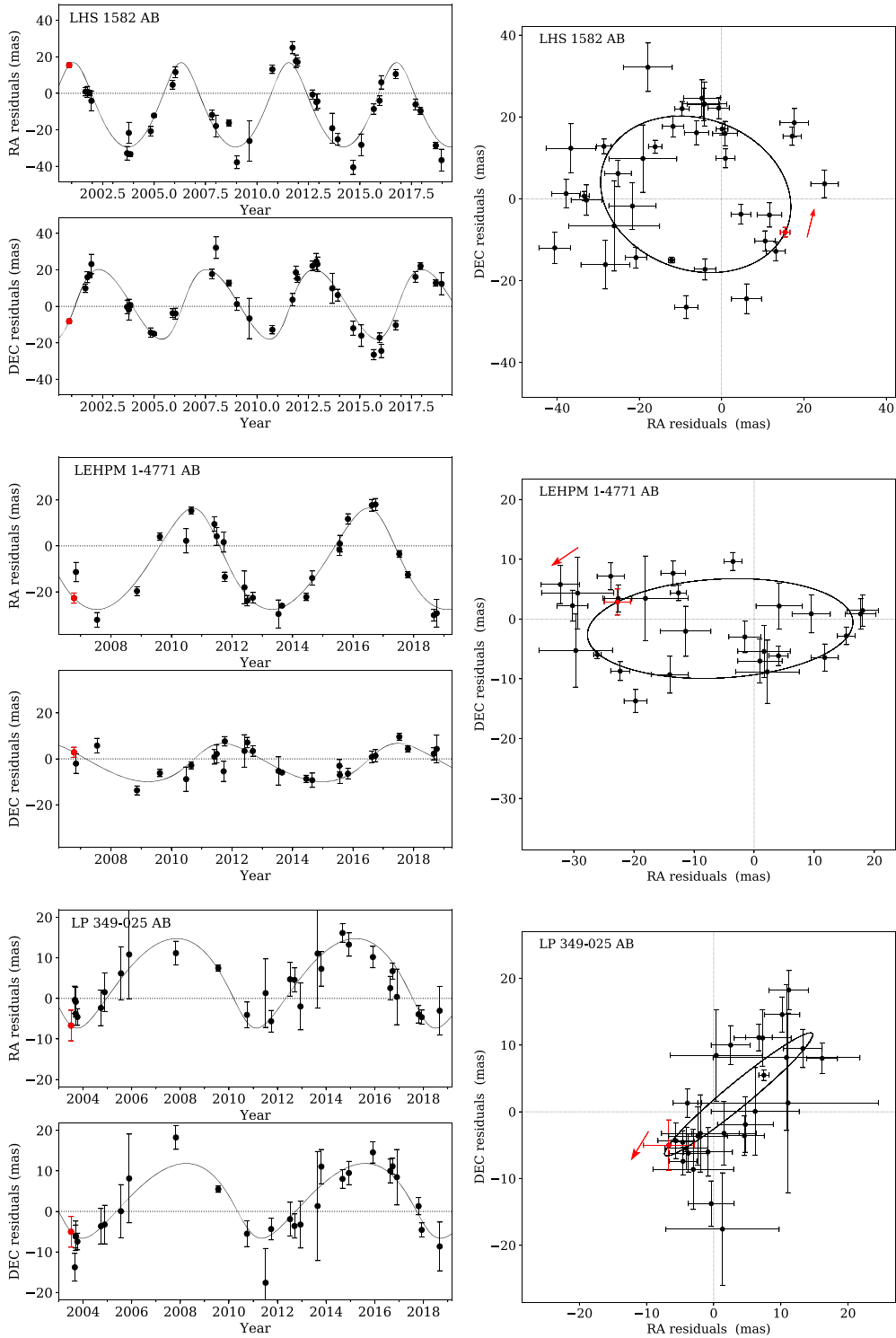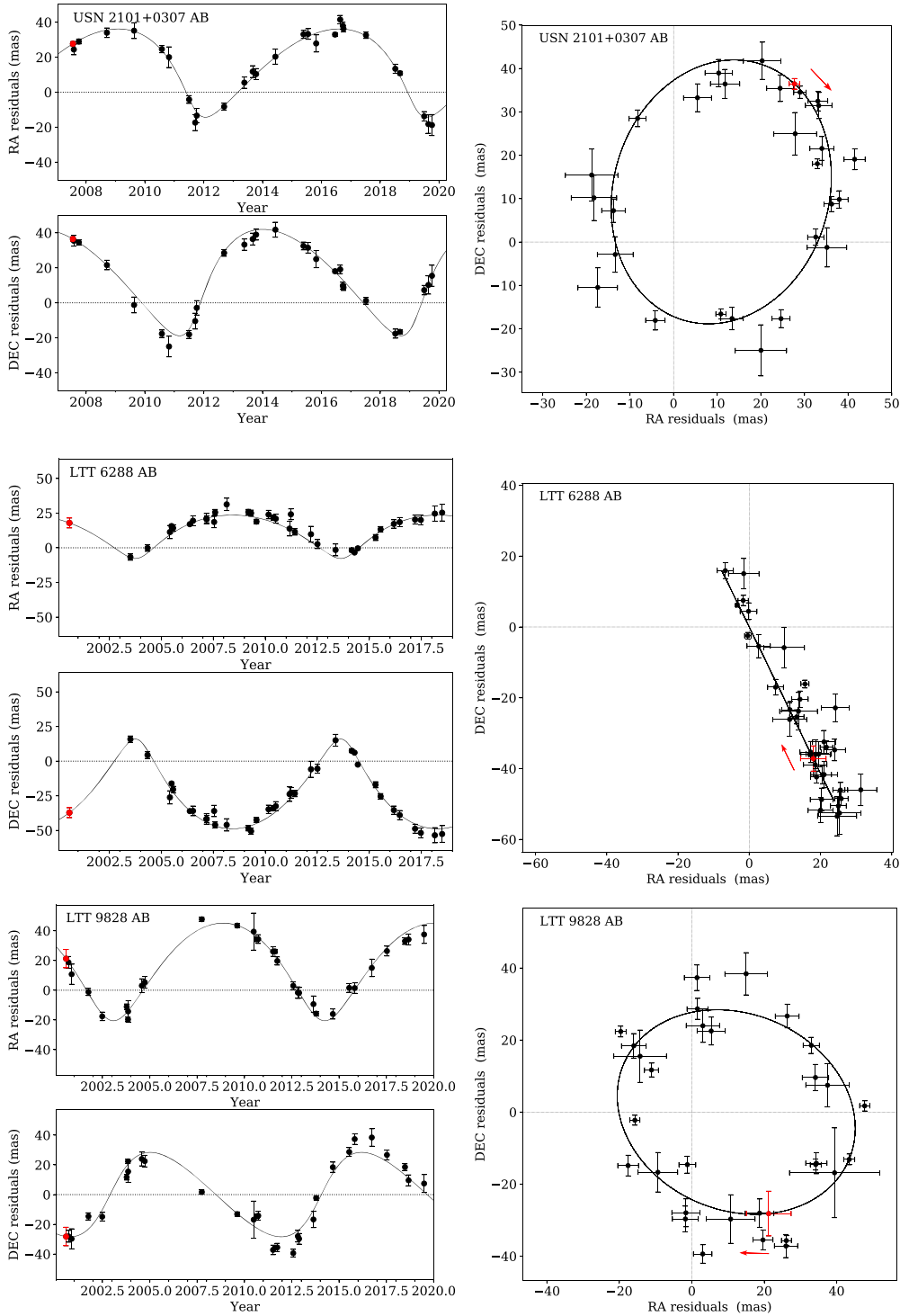[8] Appendix B of Dieterich et al. (2018) illustrates the mechanics of photocentric orbits.

Figure 1. Astrometric residuals, after proper motion and parallax have been removed, for three nearby red dwarf systems showing perturbations indicative of orbiting companions. In each panel, the solid line represents the orbit fit to that system's photocentric motion, for which the best-fit elements are given in Table 3. The first epoch is marked with a red point, and the red arrow indicates the direction of motion. In the right column, north is up, and east is to the right. These systems have well-known solutions in the literature, making them calibration systems for our observations and fitting routine. Top to bottom: GJ 748 AB ($P_{\rm orb}$ = 2.49 yr), GJ 1005 AB (4.56 yr), and GJ 234 AB (11.16 yr).

quite robust, with orbital periods of 5.23–11.17 yr and errors of only 0.02–0.19 yr. Observations of these systems at the CTIO/ SMARTS 0.9 m telescope will continue in order to improve the orbital elements further.

7. Comparison of Gaia DR2 and RECONS Astrometry Results

The Orbital Architectures project (Section 2) requires nearby multiples with months-long orbital periods, as well as years-

Figure 2. Astrometric residuals, after proper motion and parallax have been removed, for three nearby red dwarf systems showing perturbations indicative of orbiting companions. In each panel, the solid line represents the orbit fit to that system's photocentric motion, for which the best-fit elements are given in Table 3. The first epoch is marked with a red point, and the red arrow indicates the direction of motion. In the right column, north is up, and east is to the right. Top to bottom: LHS 1582 AB (P_{orb} = 5.23 yr), LEHPM 1–4771 AB (5.79 yr), and LP 349–025 AB (7.37 yr).

long periods from the RECONS astrometry program (as in Section 6). With this in mind, in our comparisons with DR2, we search for evidence of how unresolved multiples' photocentric orbital motion affects their DR2 solutions, with the intention of discerning criteria to identify new potential unresolved multiples. A new era of space-based astrometry has been initiated by ESA's Gaia mission (Gaia Collaboration et al. 2016), and with the 2018 April release of 1.7 billion parallaxes from Gaia's first 22 months of observations (DR2; Gaia Collaboration et al. 2018), the RECONS team now has an accurate but short-term yardstick against which to compare our own results. Both RECONS and Gaia provide proper motions

Figure 3. Astrometric residuals, after proper motion and parallax have been removed, for three nearby red dwarf systems showing perturbations indicative of orbiting companions. In each panel, the solid line represents the orbit fit to that system's photocentric motion, for which the best-fit elements are given in Table 3. The first epoch is marked with a red point, and the red arrow indicates the direction of motion. In the right column, north is up, and east is to the right. Top to bottom: USN 2101+0307 AB (P_{orb} = 7.53 yr), LTT 6288 AB (10.10 yr), and LTT 9828 AB (11.58 yr).

and parallaxes, but RECONS also provides orbital and multiplicity information not yet presented in the Gaia results. Each DR2 solution is computed by fitting a five-parameter single-star astrometric model for that source (Lindegren et al. 2018), and each entry in DR2 includes additional parameters describing the quality of the observations and the subsequent astrometric fit. Eventually, all multiples with separations less

than ~100 mas are expected to be unresolved to the point where only the photocenter (not individual components) is detected (Lindegren et al. 2018). In DR2, multiples with separations greater than 0."5 tend to be well resolved (Arenou et al. 2018).

In the sections that follow, we compare the RECONS astrometry results to those of Gaia DR2 for M dwarfs within

14

Table 3
Elements for the Nine Photocentric Orbits Presented in Figures 1–3

Name (1)	(2)	R.A. J2000.0 (3)	Decl. J2000.0 (4)	π (mas) (5)	μ_{RA} (mas yr^{-1}) (6)	μ_{DEC} (mas yr^{-1}) (7)	P (yr) (8)	a (mas) (9)	e (10)	i (deg) (11)	Ω (deg) (12)	ω (deg) (13)	T_0 (yr) (14)
New Systems													
LP 349–025 AB	*	00 27 55.99	+22 19 32.3	66.31 ± 1.48	397.6 ± 0.2	−161.9 ± 0.2	7.37 ± 0.19	14.63 ± 1.34	0.38 ± 0.16	97.47 ± 5.20	49.77 ± 4.29	145.06 ± 27.20	1996.05 ± 0.50
LHS 1582 AB	*	03 43 22.08	−09 33 50.9	47.62 ± 0.95	404.0 ± 0.1	308.1 ± 0.1	5.23 ± 0.02	23.70 ± 0.68	0.27 ± 0.05	143.95 ± 4.39	111.99 ± 6.57	14.90 ± 12.53	1995.82 ± 0.13
LTT 6288 AB	*	15 45 41.62	−43 30 29.0	48.22 ± 0.72	−272.2 ± 0.1	−366.1 ± 0.1	9.87 ± 0.06	36.20 ± 1.14	0.51 ± 0.06	89.95 ± 0.80	154.16 ± 1.00	191.57 ± 4.37	1994.01 ± 0.18
USN 2101+0307 AB	*	21 01 04.80	+03 07 04.7	52.91 ± 0.91	1009.2 ± 0.1	−29.6 ± 0.2	7.53 ± 0.05	33.69 ± 1.64	0.55 ± 0.05	36.71 ± 4.63	172.22 ± 8.85	57.17 ± 8.64	2004.14 ± 0.12
LEHPM 1–4771 AB	*	22 30 09.41	−53 44 55.5	64.35 ± 0.99	−64.4 ± 0.2	−739.7 ± 0.1	5.79 ± 0.06	22.39 ± 0.98	0.30 ± 0.07	122.49 ± 2.31	87.94 ± 2.49	32.28 ± 15.86	2005.29 ± 0.28
LTT 9828 AB	*	23 59 44.77	−44 05 00.3	58.87 ± 1.14	−33.4 ± 0.1	256.6 ± 0.1	11.17 ± 0.07	34.65 ± 0.90	0.38 ± 0.04	33.95 ± 4.40	123.78 ± 6.68	141.01 ± 10.11	1991.74 ± 0.24
Calibration Systems													
GJ 1005 AB	*	00 15 28.07	−16 08 01.8	169.52 ± 0.97	597.4 ± 0.2	−605.6 ± 0.1	4.56 ± 0.01	60.04 ± 1.06	0.32 ± 0.03	143.51 ± 2.14	60.78 ± 3.50	166.06 ± 6.28	1999.93 ± 0.06
	Ben16						4.56 ± 0.01		0.36 ± 0.01	146.1 ± 0.2	62.8 ± 0.4[a]	166.6 ± 0.5[a]	1995.36 ± 0.01
GJ 234 AB	*	06 29 23.39	−02 48 48.8	241.82 ± 1.21	699.7 ± 0.7	−693.0 ± 0.4	16.63 ± 0.14	294.94 ± 2.49	0.35 ± 0.01	54.26 ± 0.38	31.58 ± 0.61	43.55 ± 2.13	1999.38 ± 0.19
	Ben16						16.62 ± 0.03		0.38 ± 0.01	53.2 ± 0.1	30.60 ± 0.1[a]	40.4 ± 0.1[a]	1999.27 ± 0.01
GJ 748 AB	*	19 12 14.60	+02 53 11.0	99.89 ± 1.08	1787.7 ± 0.1	−502.2 ± 0.1	2.49 ± 0.01	29.01 ± 0.96	0.43 ± 0.05	131.00 ± 3.51	161.69 ± 3.99	142.07 ± 7.81	2002.97 ± 0.01
	Ben16						2.47 ± 0.01		0.45 ± 0.01	131.6 ± 0.3	179.6 ± 0.2[a]	207.3 ± 0.4[a]	1995.86 ± 0.01

Notes. Orbits were fit simultaneously with proper motion and parallax to RECONS astrometry data using the routine of Dieterich et al. (2018). Three systems are calibration systems, fit using the same routine as the science systems above. For these cases, the reference for the values appears to the right of the system name: * = this work, Ben16 = Benedict et al. (2016). Semimajor axis (a) is not included for the Ben16 orbits because that work fit the systems' relative orbits, whereas ours fits the photocentric orbits; hence, that parameter is not comparable.

[a] Angle rotated 180° to match the corresponding orientation for a photocentric orbit, as Benedict et al. (2016) reported the relative orbits.

25 pc using the DR2 astrometric fit quality parameters to form criteria for blindly selecting potential unresolved multiples. Section 7.1 introduces the sample of 542 nearby red dwarf systems and our procedure for matching them to DR2 sources. Section 7.2 compares the RECONS and DR2 parallaxes, and Section 7.3 compares the astrometric fit quality of unresolved multiples to resolved and single sources, where we define "cutoff" values for systems likely to be multiple. Section 7.4 briefly discusses the systems missing from Gaia DR2. Finally, other works selecting unresolved multiples from DR2 are discussed in Section 7.5.

7.1. Preparing the Comparison Sample and Matching to DR2

The systems we compare to Gaia DR2 are M dwarfs within 25 pc, as determined by one or both of RECONS and DR2 parallax $\pi \geqslant 40$ mas. These 542 systems, as listed in Table 2, include those listed in Table 1 with distances within 25 pc, as well as several hundred additional 25 pc members previously published in the *Solar Neighborhood* series. Column 4 of Table 2 gives the RECONS parallax, noted in column 5 as either a new value (asterisk) or previously published value (reference given); we compare this parallax to the DR2 parallax of column 6. Columns 7–14 reproduce the astrometric fit parameters and G magnitude from DR2 that we investigate in more detail in Section 7.3. Column 15 notes the system classification if there is evidence that it is not single: individual component of a resolved multiple ("res"), unresolved multiple ("unr"), or system with a perturbation in its RECONS astrometric residuals ("PB"). Column 16 marks those meeting all of our criteria for potential unresolved multiplicity (described in Section 7.3).

Comparing RECONS to Gaia DR2 parallaxes first requires carefully matching targets between these two catalogs. Because a key aspect of this analysis involves comparing systems with differing degrees of poor astrometric results in DR2 and multistar systems that may or may not be resolved by either catalog, care was taken to ensure that even systems without full five-parameter solutions in DR2 were considered in the pool of potential matches. Starting with the full DR2 catalog extracted from the CDS/VizieR (Ochsenbein et al. 2000), with no cuts for quality, the matching proceeded as follows.

1. For each RECONS result's R.A. and decl. (J2000), find all DR2 solutions within a $1''0$ radius. The DR2 solutions' coordinates were converted to J2000 (computed automatically by VizieR) and ranked by proximity to the RECONS target.

2. Any DR2 solution within $\sim 2''$ of the RECONS solution on the sky and with a parallax within 10 mas of the RECONS parallax was automatically considered a match. The vast majority of targets fell into this category.

3. For RECONS systems with no obvious DR2 source as described above, nearby DR2 sources lacking five-parameter solutions were carefully considered. Where possible, their B_G and R_G magnitudes[9] were checked for similarity to V and I, respectively, and their positions were compared in Aladin to images from 2MASS and DSS2. This process identified several dozen targets with DR2 sources lacking full solutions.

4. If the system was flagged in the RECONS catalog as having a perturbation in its astrometric residuals and/or an orbit fit, the potential matches within the $1''0$ radius were also screened to identify any match to the secondary component. Some secondary matches were clear by their proper motion and parallax matching the primary star, but many others were missing full five-parameter solutions (i.e., had no proper motion and parallax). When no secondary component was apparent within $1''0$, an additional search was performed by eye within $3''0–5''0$ using Aladin to visualize the DR2 catalog on background images from 2MASS and DSS2. When no secondary companion was found using these strategies, the system was flagged as an unresolved multiple.

7.2. Comparison of Parallaxes

We then compare the parallaxes of the targets common to these two catalogs in Figure 4, with the full table of these values given in Table 2. The sample has been divided into single stars, resolved components, and unresolved multiples. In the analysis that follows, all systems are presumed single unless the literature or our own observations indicate otherwise. "Resolved components" are DR2 entries corresponding to individual stars in binary or multistar systems. Due to their wide separations, even the nearest of these targets are not expected to have detectable orbital motion over the time of DR2 observations, making these systems effectively single stars for the purposes of this comparison; in case any differences do become evident, however, in this work, we have plotted these systems in a lighter shade of blue to distinguish them somewhat from systems with no known bound companions.

A 1:1 line has been plotted in the left panel of Figure 4 to indicate parallaxes with perfect agreement. The agreement between RECONS and DR2 parallaxes is generally quite good, with no obvious systematic differences with distance. The systems that fall furthest from the 1:1 line tend to be unresolved multiples. The distribution of differences for each set is plotted in the right panel of Figure 4, where each system's parallax difference has been scaled by its RECONS parallax and expressed as a percentage of that value. Here the difference is clearer between the distribution of unresolved multiples and that of single stars (combined with resolved companions): both are strongly peaked at zero, indicating many systems with good parallax agreement, but the unresolved multiples distribution is broader, representing more systems with discrepant parallaxes. The result is that the systems with a parallax difference of $\sim 10\%$ or greater tend to be unresolved multiples rather than single stars or resolved companions. On this basis, we regard the outlier "single" stars as potential unresolved multiples as well.

This scenario occurs because the model employed by Gaia to fit the astrometric data for DR2 is that of a single star; thus, it characterizes only proper and parallactic motions of the source, whereas most nearby unresolved multiples exhibit a third type of motion—orbital motion. This additional motion could mimic linear proper motion enough to mislead the astrometric fit, changing the proper-motion and parallax results (hence the discrepant values in Figure 4). This would occur in cases of long orbital periods that are not completely observed, orbits that are very eccentric, or orbits oriented nearly edge-on to the

---

[9] The Gaia DR2 magnitudes given in that catalog as `BPmag` and `RPmag` are here referred to as B_G and R_G. In other works, they are sometimes referred to as BP and RP or B_P and R_P.
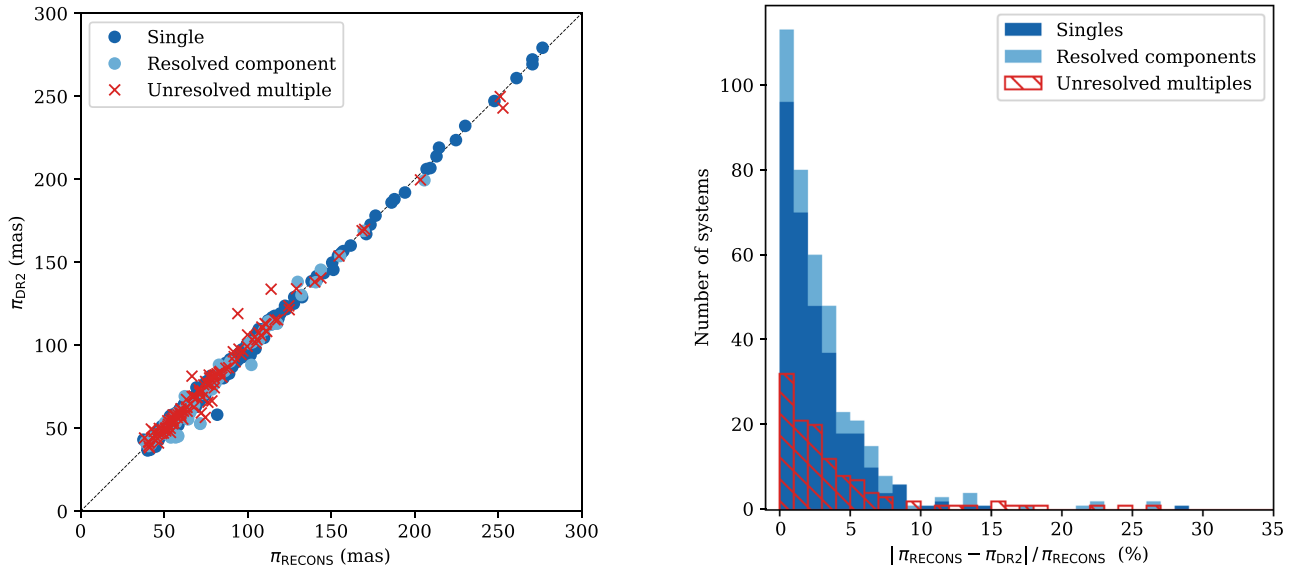
Figure 4. Parallax comparisons of RECONS astrometry to Gaia DR2 using M dwarfs within 25 pc, divided by their multiplicity status. Unresolved binaries or multistar systems are indicated with red symbols (left panel) and hatched bars (right panel), resolved components of multistar systems are light blue dots and bars, and presumed single stars are dark blue dots and bars. Left panel: RECONS parallax vs. DR2 parallax, with the dashed black line indicating the position of perfect agreement between those quantities. Right panel: difference (absolute value) between RECONS and DR2 parallax values, scaled by the corresponding RECONS parallaxes and expressed as percentages of those values. The singles and resolved components have been combined into a single histogram here, but the bars are colored to indicate the fraction belonging to each subset.

observer. Orbital motion could also create apparent scatter about the single-star model fit that would inflate the errors in that model's parameters. This analysis motivates our comparison of the astrometric fit of DR2 and RECONS and our analysis from that comparison to identify criteria for selection of likely unresolved multiples in DR2.

7.3. Comparing Astrometric Fits of Singles and Unresolved Multiples: Cutoffs for Revealing Potential Multiples in Gaia DR2

We next compare the quality of the astrometric fit in DR2 for the single stars, resolved companions, and unresolved multiples, leveraging the same sample used in the parallax comparison in Section 7.2. The quality of the DR2 data and astrometric fits is described by several parameters given with each solution, which are listed in full in Section 14 of the Gaia DR2 documentation (Hambly et al. 2018) and described in more detail in Appendix C of Lindegren et al. (2018). In the analysis that follows, we focus on a subset of eight of those parameters, four of which we find useful for selecting unresolved multiples and four of which were of interest but we find to be not useful. Described briefly (and with the notation used in Figures 5 and 6 given in parentheses), these parameters are as follows.

1. `parallax_error` (σ_π): standard uncertainty in the parallax, given in milliarcseconds.
2. `astrometric_gof_al` (goodness of fit): describes the quality of the astrometric fit, computed as a function of the reduced χ^2 of the fit—i.e., `astrometric_chi2_al` and the degrees of freedom (using only `astrometric_n_good_obs_al`). This function is constructed such that these values follow a normal distribution centered around zero with a standard deviation of 1.0.

3. `ruwe`: renormalized unit weight error (RUWE), representing the quality of the astrometric fit as a single dimensionless value. This parameter is analogous to `astrometric_excess_noise` (described below) but expressed in a dimensionless form intended to be easier to interpret. It has been normalized to correct for quality issues in very bright and very faint sources and as a function of source color (Lindegren 2018).
4. `astrometric_excess_noise_sig` (significance of excess noise): significance of `astrometric_excess_noise` (described below), constructed to statistically resemble the positive half of a Gaussian distribution centered around zero with a standard deviation of 1.0.
5. `astrometric_excess_noise` (excess noise): the difference between the DR2 data and the astrometric fit, given as the angle between these quantities on the sky. For each source, this value is used to indicate the noise of each observation contributing to the final solution. Values of zero indicate good astrometric fits, with positive increasing values indicating statistically higher-than-expected residuals.
6. `astrometric_n_good_obs_al` (N_{good}): number of observations that were not downweighted in the computation of the astrometric solution, analogous to the number of frames in RECONS data.
7. `astrometric_n_bad_obs_al` (N_{bad}): number of observations that were downweighted in the computation of the astrometric solution, thus contributing little to the astrometric solution.
8. In addition to the above seven parameters, we also calculate `astrometric_n_bad_obs_al` divided by `astrometric_n_good_obs_al` ($N_{\mathrm{bad}}/N_{\mathrm{good}}$) for each point, as Arenou et al. (2018) suggested that this quantity could be elevated for unresolved multiples.
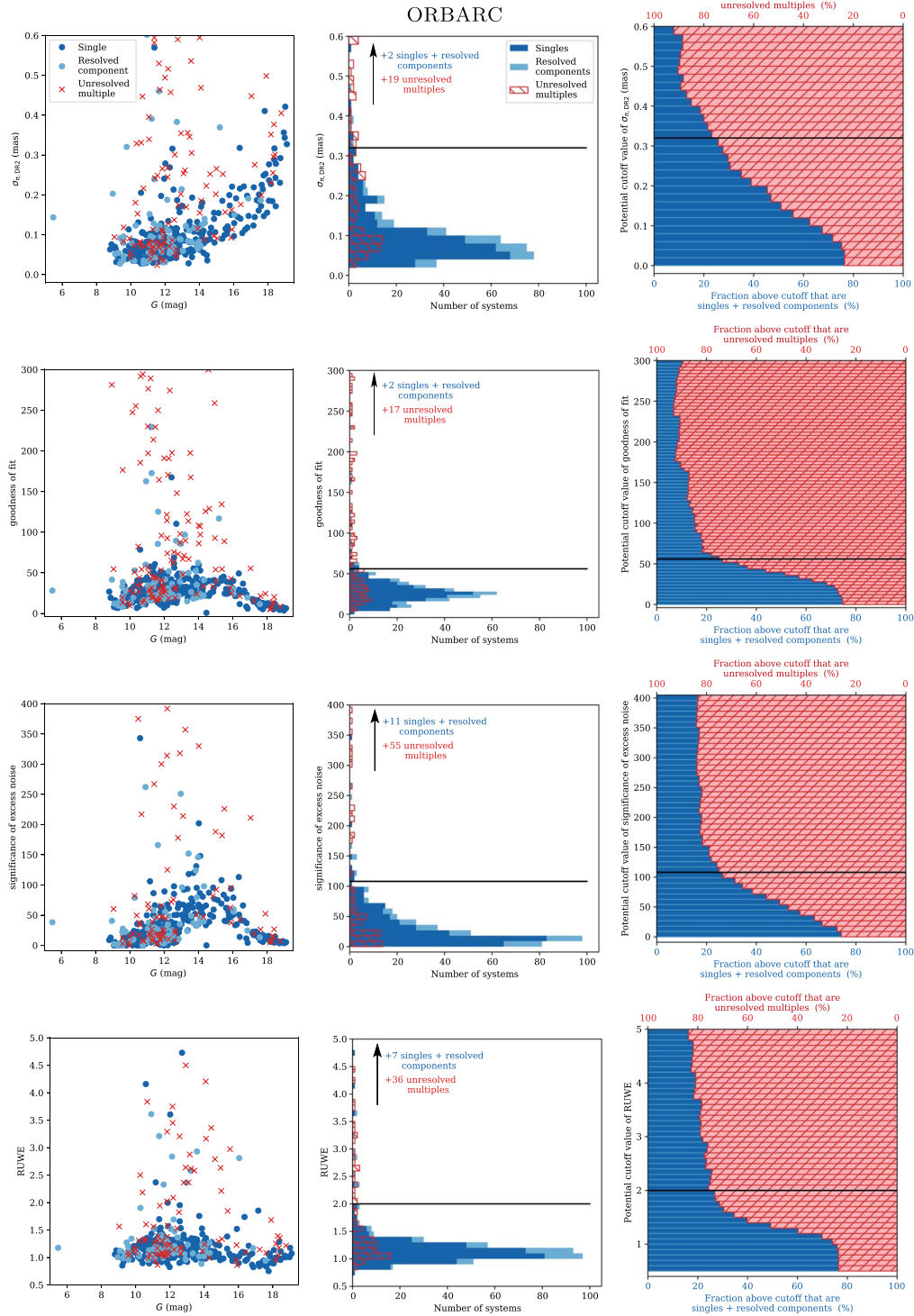
16

Figure 5. Astrometric fit parameters in DR2 that are useful for selecting potential unresolved multiples. In all panels, the color scheme is the same as in Figure 4. Left column: parameters for single systems, resolved components, and unresolved multiples in Gaia DR2, plotted against their Gaia G magnitudes. The unresolved multiples tend to have higher values of these fit parameters independent of their G magnitude, indicating their poor astrometric fits in DR2. Middle column: distributions of these parameters for systems in the left column, separated again by multiplicity status. Systems with values outside these plots are noted with the arrow and text in each panel. Although both distributions are peaked at low values of each parameter, the distribution of unresolved multiples extends to higher values. Right column: potential cutoff values for each parameter, showing the fraction of systems above each cutoff belonging to singles and resolved components (blue) and unresolved multiples (red). The cutoff values above which 75% of our systems are unresolved multiples (Section 7.3) are indicated with a horizontal black line.

To establish criteria for likely multiplicity, we plot the values of these eight quantities for the single stars, resolved components, and unresolved multiples shared by the Gaia

DR2 and RECONS 25 pc samples. These visual comparisons are presented in the left columns of Figures 5 and 6. In each of these plots, the DR2 parameters are set against the G magnitude
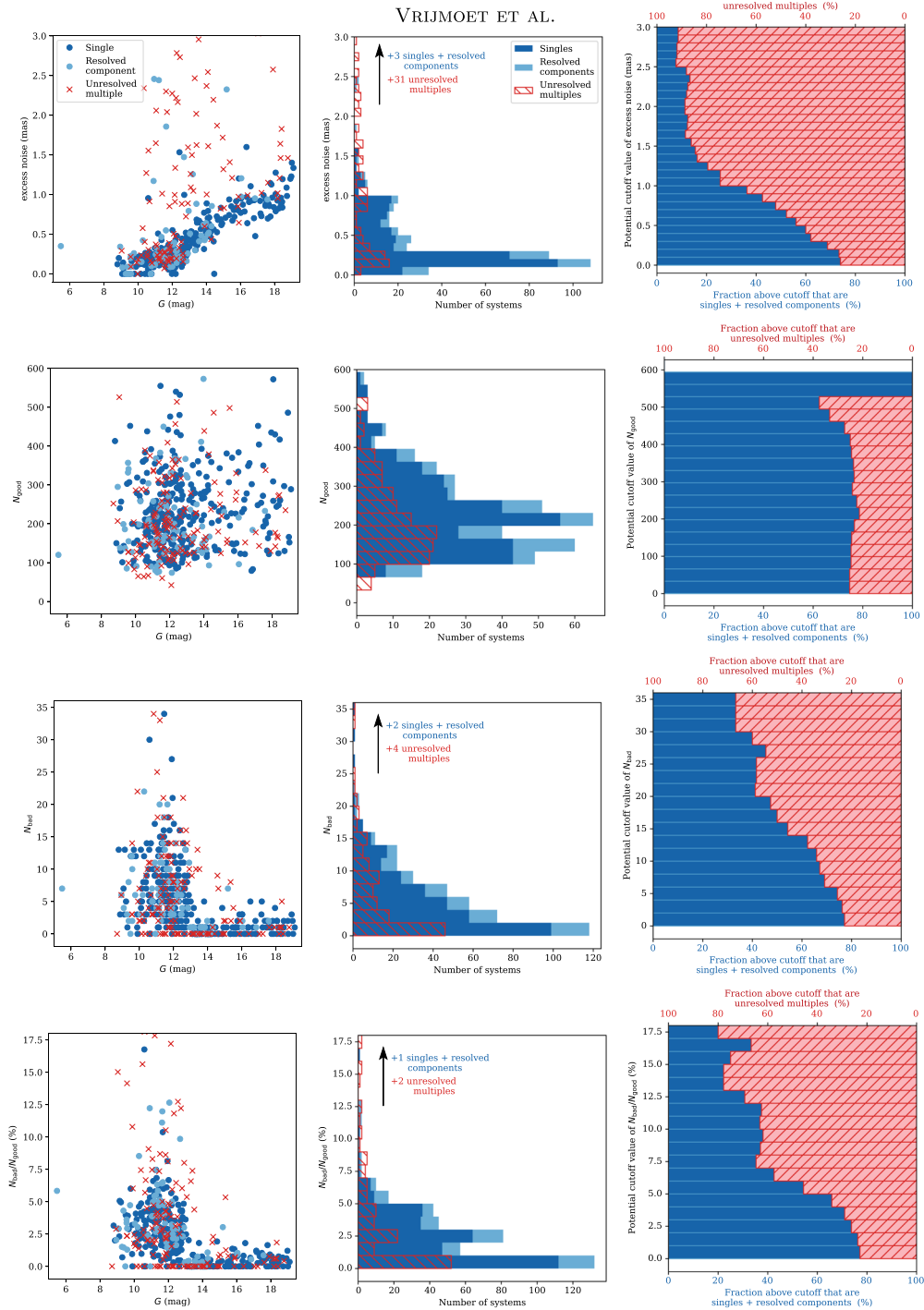
Figure 6. Four quantities in DR2 that are less useful for choosing potential unresolved multiples. The color schemes and columns are the same as for Figure 5, and any systems with values exceeding these ranges are noted with an arrow and text in each panel. For these quantities, the distributions of single and unresolved systems do not differ as significantly as those in Figure 5, making them less useful for identifying potential unresolved systems. Excess noise (`astrometric_excess_noise`) does show a distinction between singles and multiples, but it is less useful than the very similar `astrometric_excess_noise_sig` because it strongly depends on G magnitude (faint singles have values similar to brighter unresolved multiples).

of each source, allowing easy identification of any trend with magnitude, as faintness may degrade the astrometric fit even for single stars.

Figure 5 presents four astrometric parameters that exhibit clear differences between the distributions of unresolved multiples and single stars/resolved components. These distribution differences have been judged by eye using the three

types of diagnostic plots in Figure 5, as the differences are clear and the goal of this work is to identify the four most useful parameters (rather than an all-inclusive list of every useful parameter). In each panel of the left column, the single stars and resolved components cluster primarily at low values of the given DR2 fit parameter, indicating high-quality fits, whereas the unresolved multiples show a greater spread and thus much
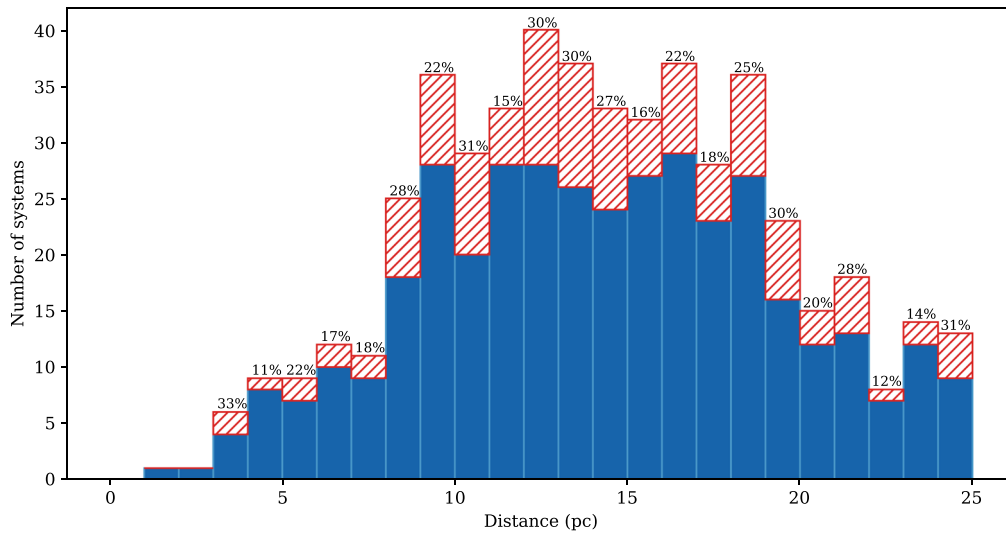
Figure 7. Number of systems in 1 pc shells outward from the Sun. Blue bars indicate single stars, red hatched bars are the multiples unresolved in Gaia DR2, and black labels indicate the multiplicity in each 1 pc bin based on known unresolved multiples as a fraction of each bin's total. For bins with ≳13 systems, the multiplicity is similar to that observed in volume-complete surveys such as Winters et al. (2019), which reported 27% multiplicity. Although the dropoff of systems past ∼13 pc indicates that our survey is not volume-complete past that distance, the average multiplicity for those bins is 26%; therefore, our incompleteness is not biased toward single stars or multiples.

more variation in fit quality. Of the systems with poor fits indicated by these parameters, the majority are unresolved multiples. Note that in all columns, there are many multiples off the tops of each plot, and only a few singles. The plot limits have been set to prioritize the clarity of the distributions. To clarify these trends, the middle column of Figure 5 illustrates these distributions as histograms, with bins assigned by the Freedman–Diaconis rule applied over the range shown to accommodate the often non-Gaussian nature of these distributions and the outliers in each set. The distributions of each set of targets are not the same for each DR2 parameter, as each of those values is calculated differently and describes a different aspect of the astrometric model fit.

To determine a useful "cutoff" value for each parameter, we define cutoffs that provide that 75% of a population will be multiples. To define these criteria, in the right column of Figure 5, we plot the potential cutoff values for each parameter against the "set composition" of the targets with values above each potential cutoff. For the systems exceeding each potential cutoff value (each value on the vertical axis), the bars at that coordinate indicate what fraction are unresolved multiples and what fraction are single stars or resolved companions. A parameter that is useful for selecting potential unresolved multiples would have some point at which the balance of systems above that cutoff is dominated by the unresolved multiples, making it overwhelmingly likely that any selected system above that point is not single.

This method is chosen in lieu of a Gaussian characterization and standard deviation–based criteria because most of these distributions do not follow normal distributions and our 25 pc sample is not volume-complete. Figure 7 illustrates the number of systems in our sample in 1 pc shells extending outward from the Sun, with the fraction of unresolved multiples indicated by red bars and percentage labels. As the shells extend outward in equal-radius steps, their contained volume increases; thus, we expect that the number of systems in each shell would increase accordingly. This trend is indeed followed until ∼13 pc, where the number of systems in subsequent shells begins to fall, indicating volume incompleteness at these distances. Despite

the paucity of systems past 13 pc, however, the fraction of multistar systems in each bin is 20%–30% (average 26%), consistent with the more robust multiplicity for M dwarfs measured by Winters et al. (2019). The unresolved multiples are therefore not systematically over- or underrepresented with distance. Furthermore, plotting the DR2 parameters against these distances does not reveal any distance-dependent trend, eliminating the possibility that the paucity of systems at large distances will significantly bias the positions of the cutoffs.

Finally, we note that the unresolved multiples among the missing systems would likely have small-amplitude orbital motion or longer orbital periods, as these systems' greater distances would shrink the scales of their apparent orbits. Then these missing systems, if they were included in our sample, would likely have good astrometric fits in DR2 and add more to the sizes of the peaks of the distributions in Figures 5 and 6, rather than the outliers. The result would be a minimal effect on our definitions of the cutoff points.

Choosing the cutoffs as the points where at least three out of four systems (75%) above that point are unresolved multiples, we arrive at the following criteria:

1. `parallax_err` ⩾ 0.32 mas for $G \lesssim 18$ (⩾0.40 for $G \gtrsim 18$),
2. `astrometric_gof_al` ⩾ 56.0,
3. `astrometric_excess_noise_sig` ⩾ 108.0, and
4. `ruwe` ⩾ 2.0.

Targets meeting all four of these criteria are marked with check marks in column 16 of Table 2. For `parallax_err`, this cutoff must include the caveat that systems fainter than $G \sim 18$ show elevated values regardless of duplicity, making a more appropriate cutoff in that region `parallax_err` ⩾ 0.40 mas. Such brightness dependence is also the reason we recommend `astrometric_excess_noise_sig` rather than `astrometric_excess_noise`; although both show clear points where the unresolved multiple distribution dominates, the dimensionless `astrometric_excess_noise_sig` is more controlled with respect to G (see Figure 5, third row), whereas `astrometric_excess_noise` (Figure 6, first

row) rises continuously with magnitude in the brightness range we examine here. The values presented above are likely overestimates, as many systems currently marked "single" have not had sufficient observations in our astrometry to fully rule out the existence of a bound companion. Some of those systems may later be revealed as unresolved binaries.

In presenting these "cutoff" values, we must emphasize that they do not represent dividing lines between single and unresolved multiple systems in the DR2 results. This investigation suggests that systems with values exceeding these points are likely to be unresolved multiples, but also that systems with values below these points may be multiple or single; those entries are ambiguous at best. The astrometry of an unresolved multiple would match a single-star model in cases where the brightness ratio is large or zero (which is why Arenou et al. 2018 found an insignificant difference in astrometric fit between single stars and unresolved multiples with small Δmag) or the orbital period is much longer than 22 months.

We explored several additional parameters, and in Figure 6, we present four quantities that we found to be not as useful as expected for selecting unresolved multiples. This judgment is made by eye using the middle and right columns of Figure 6. The quantity `astrometric_excess_noise` (first row of Figure 6) shows a strong difference between the distributions of unresolved multiples and single stars (and resolved components), but its dependence on the G magnitude makes it less useful for distinguishing potential multiples than the similar parameter `astrometric_excess_noise_sig`. The parameters `astrometric_n_good_obs_al` and `astrometric_n_bad_obs_al` show very little distinction between the distributions of unresolved multiples and single stars. Finally, dividing the bad observations by the good observations (as suggested by Arenou et al. 2018) also produces a rather weak trend (visible in the third row of Figure 6).

7.4. Systems Missing from Gaia DR2

In addition to systems with poor astrometric fits as indicated by the fit parameters, several systems in Gaia DR2 are missing parallaxes (i.e., have a two-parameter solution rather than a five-parameter solution) or are missing from that catalog entirely. These results indicate targets for which the five-parameter solution was an exceptionally poor fit (Lindegren et al. 2018). For the nearby red dwarfs, 42 of these targets appear in Table 2 with blank spaces in their DR2-specific fields. These systems represent 7.2% of our 25 pc sample.

Astrometric fits poor enough to merit exclusion from DR2 could be multiples with photocentric orbital motion, and on this basis, we have marked these systems as "suspicious" in column 16 of Table 2. Of the 42 of these systems in the 25 pc sample, 27 (64%) have unresolved companions or astrometric perturbations noted in Table 2, and four are resolved components of multiple systems. In addition to multiplicity, Arenou et al. (2018) cited high proper motion as a primary reason for stellar point sources to be missing DR2 solutions, but only four of our nonmultiple missing systems meet their benchmark of 600 mas yr^{-1}: SSS 1444–2019 (3495.1 mas yr^{-1}), 2MA 0251–0352 (2149.7 mas yr^{-1}), LHS 1918 (606.0 mas yr^{-1}), and GJ 273 (3732.1 mas yr^{-1}). We therefore note that the remaining seven are particularly worthy of follow-up investigation regarding their multiplicity status.

7.5. Comparison to Similar Works

Other published works selecting multiples from DR2 have focused on the proper-motion anomaly (Brandt 2018; Kervella et al. 2019), or the difference in a target's proper motion measured over a few years and its motion as computed over a decades-long temporal baseline. The Gaia DR2 catalog presents the opportunity to calculate this anomaly because of its nearly 25 yr temporal separation from the Hipparcos astrometric mission, which measured positions, proper motions, and parallaxes of more than 100,000 stars from 1989 to 1993 (Perryman et al. 1997; van Leeuwen 2007). Systems with significant proper-motion anomalies are likely unresolved multiples, as a system with a bound companion inducing orbital motion will have nonlinear proper motion, i.e., acceleration.

Brandt (2018) renormalized the Hipparcos and Gaia DR2 errors and presented a catalog of proper-motion anomalies for systems common to these two catalogs, but the faintness limits of Hipparcos limit the overlap between this catalog and our 25 pc sample to 59 systems. The faintest system in Brandt (2018) has $G = 12.31$, whereas our catalog extends to $G = 19.01$. Brandt (2018) did not suggest a benchmark value to flag accelerating systems and instead advocated a case-by-case approach. Of the 59 targets common to that catalog and our 25 pc sample, only seven have proper motions that differ by more than 20% in their comparisons, and we confirm that four of those are unresolved multiples; we suspect the other three will turn out to be multiples as well. Our method of DR2 parameter cutoffs (Section 7.3) identifies eight likely unresolved multiples from the 59 common targets, with seven being confirmed multiples, but only two of those systems are flagged by the 20% acceleration search above.

Kervella et al. (2019) computed the Hipparcos–DR2 proper-motion anomaly similarly to Brandt (2018) but limited their core sample to systems within 50 pc. By taking into account the radial velocities of their systems (with ∼70% of these radial velocities not from the DR2 entries), they are able to set limits on the masses of potential companions to the anomalous systems. As in our comparison with Brandt (2018), of the 51 systems in common between Kervella et al. (2019) and our 25 pc catalog, our DR2 criteria identify eight potential multiples. Seven of these are already confirmed unresolved multiples, and seven (not the same subset) are flagged by Kervella et al. (2019) as likely binaries. In addition to these, Kervella et al. (2019) flagged nine more systems as likely binaries (for a total of 16 of the 51) that do not meet our DR2 criteria; four of these are confirmed multiples (for a total of 11 confirmed of their 16 flagged).

These searches suggest that both methods are effective at selecting likely unresolved multiples, but they are not sensitive to the same orbits. Our approach using the DR2 fit quality seeks the systems with significant motion on DR2's 22 month observing timescale and is poorly sensitive to systems with decades-long orbits, whereas the Brandt (2018) catalog is likely more sensitive to systems with significant motion on those decades-long timescales because it hinges on the Hipparcos–DR2 25 yr baseline. We also note that our approach using Gaia DR2 parameters alone is applicable to more systems because it is not restricted by the faintness limit of Hipparcos. For those systems highlighted by Brandt (2018), however, that catalog's offered information is rich enough to constrain the dynamical masses when combined with just a single measurement of

separation of the resolved components, propelling the user past the step of mapping orbits that could be decades or centuries in length (demonstrated in Brandt et al. 2019).

The RUWE merits a dedicated discussion because it is intended as a straightforward, easy way to interpret the quality of each astrometric fit to the single-star model, as has been used by some studies already to exclude (or include) multiples (e.g., Scholz et al. 2019). Provided as a lookup table several months after the DR2, `ruwe` is the reduced χ^2 normalized to counter the documented statistical trends of `astrometric_chi2_al` with G and $B_G - R_G$. The DR2 technical documentation (Lindegren 2018) suggests that solutions with `ruwe` > 1.4 indicate bad fits likely due to orbital motion, with enough confidence that it will be incorporated into the criteria for selecting unresolved multistar system candidates in Gaia's upcoming orbital motion pipeline (Pourbaix 2019). Our comparison of this parameter in Figure 5 confirms that targets with high `ruwe` values are more likely to be unresolved multiples than single stars. This result is confirmed for the FGK stars by Ziegler et al. (2020), who detected stellar companions with SOAR speckle interferometry for 84% of their 135 FGK systems with `ruwe` > 1.4. In a multiplicity-focused study, Jorissen (2019) also found a correlation between duplicity and `ruwe` using a sample of bright spectroscopic multiples from SB9. Although those authors cautioned that the link may not be sustained for multiples fainter than their sample of $6 \leqslant G \leqslant 10$, our similar work here uses a large number of systems with $G \sim 10$–20. We recommend `ruwe` as an effective way to select many unresolved multiples, but we note that its given format as a separate lookup table only accessible through the ESA website makes it less convenient to use than the other astrometric parameters, which are delivered alongside the DR2 solutions everywhere that catalog is accessible.

8. Validation of the Unresolved Multiples via SOAR Observations

Using the criteria described in Section 7, we have added 114 nearby likely multistar red dwarfs to a sample that we are observing with speckle interferometry at the SOAR telescope. These targets include most of the 97 marked in column 16 of Table 2 (those within the brightness and airmass limits of SOAR), supplemented by many that meet only a subset of those criteria. The speckle interferometry is carried out using the high-resolution camera mounted on the adaptive optics module on SOAR (HRCam+SAM; see Tokovinin 2018). These observations will complement the long-term RECONS astrometry by mapping orbits shorter than ~6 yr through multi-epoch observations on these 25 pc M dwarfs. There is significant overlap in the target lists of the SOAR and CTIO/SMARTS 0.9 m programs, as these two facilities have the same latitude and sky coverage. Systems flagged through the Gaia DR2 parameters described above (Section 7) are well suited for this 3 yr SOAR program because only systems with appreciable orbital motion in DR2's 22 month observations will have poor astrometric fits.

Initial results have marked a promising start to this observing program, with 90% of the DR2-selected targets already observed, of which 73% have had companions detected. Several systems have also had orbital motion detected through these multi-epoch observations, demonstrating that this program is already capturing the fast orbits that are most needed to

complement the RECONS astrometric multiples. A full description of these observations and results will be presented in a forthcoming paper.

9. Conclusions

Efforts to complete the astronomical community's census of nearby red and brown dwarfs have expanded beyond RECONS since that program's inception in 1999 and will continue to expand in precision with future updates from Gaia astrometry. Considering this success, the focus of the RECONS astrometry program has shifted toward the potential for characterization of its red dwarf systems enabled by their remarkably long temporal baseline of astrometry and relative photometry (variability).

Specific results of this paper include the following.

1. We deliver the single biggest update of (and addition to) RECONS astrometry to date: 210 systems with 220 distinct proper motions and parallaxes, of which 155 are new and 65 are updates to the RECONS catalog.
2. We present nine high-quality orbits from RECONS astrometry, fit using a new technique that determines the astrometric parameters simultaneously with the orbit elements (introduced in Dieterich et al. 2018).
3. These orbits represent the beginning of a project to assemble M dwarf orbits across the entire range of that extensive spectral type, with the goal of identifying any trends (or lack thereof) in the sizes and shapes of these orbits.
4. Using a set of 542 RECONS systems (with 582 distinct parallaxes), we have defined four criteria for selection of potential unresolved multiples among nearby targets in Gaia DR2 (see Section 7.3).

These results, in particular the DR2 unresolved multiples selection criteria, can be used to hone samples for everything from stellar astrophysics to exoplanet searches. Additional observations, such as our new speckle imaging program at SOAR, will allow us to refine these DR2 criteria by identifying new unresolved multiples. The rich set of M dwarf multiples revealed by this work will be used in the Orbital Architectures project to answer fundamental questions about the formation of multistar systems. Ultimately, these systems can be either avoided or targeted in searches for planets orbiting the nearest stars.

Facility: CTIO:0.9m.

Software: GaussFit (Jefferys et al. 1987), IRAF (Tody 1986, 1993), SExtractor (Bertin & Arnouts 1996).

ORCID iDs

Eliot Halley Vrijmoet ⬥ https://orcid.org/0000-0002-1864-6120
Todd J. Henry ⬥ https://orcid.org/0000-0002-9061-2865
Wei-Chun Jao ⬥ https://orcid.org/0000-0003-0193-2187
Serge B. Dieterich ⬥ https://orcid.org/0000-0001-7210-3912

References

Alonso-Floriano, F. J., Morales, J. C., Caballero, J. A., et al. 2015, A&A, 577, A128
Arenou, F., Luri, X., Babusiaux, C., et al. 2018, A&A, 616, A17
Bartlett, J. L., Lurie, J. C., Riedel, A., et al. 2017, AJ, 154, 151
Bate, M. R. 2012, MNRAS, 419, 3115
Bate, M. R. 2015, in ASP Conf. Ser. 496, Living Together: Planets, Host Stars and Binaries, ed. S. M. Rucinski, G. Torres, & M. Zejda (San Fransisco, CA: ASP), 37
Benedict, G. F., Henry, T. J., Franz, O. G., et al. 2016, AJ, 152, 141
Bertin, E., & Arnouts, S. 1996, A&AS, 117, 393
Brandt, T. D. 2018, ApJS, 239, 31
Brandt, T. D., Dupuy, T. J., & Bowler, B. P. 2019, AJ, 158, 140
Ciardi, D. R., Beichman, C. A., Horch, E. P., et al. 2015, ApJ, 805, 16
Clements, T. D., Henry, T. J., Hosey, A. D., et al. 2017, AJ, 154, 124
Cortés-Contreras, M., Béjar, V. J. S., Caballero, J. A., et al. 2017, A&A, 597, A47
Cutri, R. M., Skrutskie, M. F., van Dyk, S., et al. 2003, yCat, 2246, 0
Davison, C. L., White, R. J., Henry, T. J., et al. 2015, AJ, 149, 106
Delfosse, X., Forveille, T., Ségransan, D., et al. 2000, A&A, 364, 217
Dieterich, S. B., Henry, T. J., Jao, W.-C., et al. 2014, AJ, 147, 94
Dieterich, S. B., Weinberger, A. J., Boss, A. P., et al. 2018, ApJ, 865, 28
Duchêne, G., & Kraus, A. 2013, ARA&A, 51, 269
Duquennoy, A., & Mayor, M. 1991, A&A, 500, 337
Fressin, F., Torres, G., Charbonneau, D., et al. 2013, ApJ, 766, 81
Furlan, E., Ciardi, D. R., Everett, M. E., et al. 2017, AJ, 153, 71
Gaia Collaboration, Brown, A. G. A., Vallenari, A., et al. 2018, A&A, 616, A1
Gaia Collaboration, Prusti, T., de Bruijne, J. H. J., et al. 2016, A&A, 595, A1
Gardner, J. P., Mather, J. C., Clampin, M., et al. 2006, SSRv, 123, 485
Halbwachs, J. L., Mayor, M., & Udry, S. 2005, A&A, 431, 1129
Hambly, N., Altmann, M., Arenou, F., et al. 2018, Gaia DR2 Documentation, https://gea.esac.esa.int/archive/documentation/GDR2/
Hartkopf, W. I., McAlister, H. A., & Franz, O. G. 1989, AJ, 98, 1014
Henry, T. J., Franz, O. G., Wasserman, L. H., et al. 1999, ApJ, 512, 864
Henry, T. J., Jao, W.-C., Subasavage, J. P., et al. 2006, AJ, 132, 2360
Henry, T. J., Jao, W.-C., Winters, J. G., et al. 2018, AJ, 155, 265
Henry, T. J., & McCarthy, D. W. 1993, AJ, 106, 773
Hosey, A. D., Henry, T. J., Jao, W.-C., et al. 2015, AJ, 150, 6
Jao, W.-C., Henry, T. J., Subasavage, J. P., et al. 2005, AJ, 129, 1954
Jao, W.-C., Henry, T. J., Subasavage, J. P., et al. 2011, AJ, 141, 117
Jao, W.-C., Henry, T. J., Winters, J. G., et al. 2017, AJ, 154, 191
Jefferys, W. H., Fitzpatrick, M. J., & McArthur, B. E. 1987, CeMec, 41, 39
Jorissen, A. 2019, MmSAI, 90, 395
Kervella, P., Arenou, F., Mignard, F., et al. 2019, A&A, 623, A72
Lindegren, L. 2018, Re-normalising the Astrometric Chi-square in Gaia D2 GAIA-C3-TN-LU-LL-124, http://www.rssd.esa.int/doc_fetch.php?id=3757412
Lindegren, L., Hernández, J., Bombrun, A., et al. 2018, A&A, 616, A2
Lurie, J. C., Henry, T. J., Jao, W.-C., et al. 2014, AJ, 148, 91
Moe, M. 2019, MmSAI, 90, 347
Moe, M., & Di Stefano, R. 2017, ApJS, 230, 15
Ochsenbein, F., Bauer, P., & Marcout, J. 2000, A&AS, 143, 23
Parker, R. J., & Meyer, M. R. 2014, MNRAS, 442, 3722
Perryman, M. A. C., Lindegren, L., Kovalevsky, J., et al. 1997, A&A, 500, 501
Pourbaix, D. 2019, MmSAI, 90, 318
Quirrenbach, A., Amado, P. J., Caballero, J. A., et al. 2016, Proc. SPIE, 9908, 990812
Ricker, G. R., Winn, J. N., Vanderspek, R., et al. 2014, Proc. SPIE, 9143, 914320
Riedel, A. R., Finch, C. T., Henry, T. J., et al. 2014, AJ, 147, 85
Riedel, A. R., Silverstein, M. L., Henry, T. J., et al. 2018, AJ, 156, 49
Riedel, A. R., Subasavage, J. P., Finch, C. T., et al. 2010, AJ, 140, 897
Scholz, R.-D., Chojnowski, S. D., & Hubrig, S. 2019, A&A, 628, A81
Skrutskie, M. F., Cutri, R. M., Stiening, R., et al. 2006, AJ, 131, 1163
Stassun, K. G., Oelkers, R. J., Pepper, J., et al. 2018, AJ, 156, 102
Subasavage, J. P., Jao, W.-C., Henry, T. J., et al. 2009, AJ, 137, 4547
Subasavage, J. P., Jao, W.-C., Henry, T. J., et al. 2017, AJ, 154, 32
Tody, D. 1986, Proc. SPIE, 627, 733
Tody, D. 1993, in ASP Conf. Ser. 52, Astronomical Data Analysis Software and Systems II, ed. R. J. Hanisch, R. J. V. Brissenden, & J. Barnes (San Fransisco, CA: ASP), 173
Tokovinin, A. 2018, PASP, 130, 035002
Udry, S., Mayor, M., Delfosse, X., et al. 2000, in IAU Symp. 200, Birth and Evolution of Binary Stars, ed. B. Reipurth & H. Zinnecker (Cambridge: Cambridge Univ. Press), 158
van de Kamp, P. 1967, Principles of Astrometry (San Francisco, CA: Freeman)
van Leeuwen, F. 2007, A&A, 474, 653
Winters, J. G., Henry, T. J., Jao, W.-C., et al. 2019, AJ, 157, 216
Winters, J. G., Irwin, J. M., Charbonneau, D., et al. 2020, AJ, 159, 290
Winters, J. G., Sevrinsky, R. A., Jao, W.-C., et al. 2017, AJ, 153, 14
Ziegler, C., Tokovinin, A., Briceño, C., et al. 2020, AJ, 159, 19